

# JGR Solid Earth

## RESEARCH ARTICLE

10.1029/2020JB021422

### Key Points:

- Mud samples from El Tatio Geyser field have high trace elemental retention capacity
- The desorption of trace elements from the mud surfaces significantly controls trace elemental cycling
- Clays can be important vectors in the transport of trace elements from land to the oceans

### Supporting Information:

Supporting Information may be found in the online version of this article.

### Correspondence to:

W. Hao,  
[whao@ualberta.ca](mailto:whao@ualberta.ca)

### Citation:

Hao, W., Mänd, K., Swaren, L., Myers, K. D., Lalonde, S., Wilmeth, D. T., et al. (2021). Trace elemental partitioning on clays derived from hydrothermal muds of the El Tatio Geyser Field, Chile. *Journal of Geophysical Research: Solid Earth*, 126, e2020JB021422. <https://doi.org/10.1029/2020JB021422>

Received 30 NOV 2020

Accepted 22 APR 2021

## Trace Elemental Partitioning on Clays Derived From Hydrothermal MudS of the El Tatio Geyser Field, Chile

Weiduo Hao<sup>1</sup> , Kaarel Mänd<sup>1,2</sup> , Logan Swaren<sup>1</sup> , Kimberly D. Myers<sup>3</sup> , Stefan Lalonde<sup>4</sup>, Dylan T. Wilmeth<sup>3</sup>, Mark Van Zuilen<sup>3</sup>, Siobhan A. Wilson<sup>1</sup> , Daniel S. Alessi<sup>1</sup> , and Kurt O. Konhauser<sup>1</sup>

<sup>1</sup>Department of Earth & Atmospheric Sciences, University of Alberta, Edmonton, AB, Canada, <sup>2</sup>Department of Geology, University of Tartu, Tartu, Estonia, <sup>3</sup>Institut de physique du globe de Paris, CNRS, Université de Paris, Paris, France, <sup>4</sup>Laboratoire Géosciences Océan, Institut Universitaire Européen de la Mer, Plouzané, France

**Abstract** Recent experimental studies have demonstrated that clay minerals (e.g., kaolinite, illite, and montmorillonite) have higher affinities for some trace elements under acidic versus alkaline conditions. This suggests that clays might be important vectors in the transport of trace elements from sites of acidic chemical weathering on land to marine depositional environments. To determine if clays behave similarly in nature, we collected water and mud (consisting of 38.5%–61.1% of kaolinite and montmorillonite) samples from boiling, low-pH, mud pools venting at the El Tatio Geyser Field (ETGF) in Chile. Based on elemental abundances in the aqueous/solid phases, we observed that mud samples collected from lower pH pools (e.g., pH = 2.42 and 3.55) have high concentration factors for anionic elements (e.g., P and As) but low concentration factors for cationic elements (e.g., Ca, Mn, and Sr), while mud samples from higher pH pools (e.g., pH = 4.87 and 5.84) display the opposite trend. Acid-base leaching experiments further reveal that increasing solution pH (to reflect downstream transport) led to the release of As and P from the mud surfaces due to increasingly negative surface charge, while decreasing pH (to determine the effects of re-acidification) released Li, Ca, Co, Sr, Mo, and Cd. Our study confirms previous experimental findings that demonstrate clay minerals can assemble a diverse inventory of trace elements during acid weathering (e.g., As) but then liberate them back into the aqueous phase as aqueous pH increases. Importantly, these observations provide a mechanism to account for the previous observations of regional As contamination in rivers downstream of the ETGF.

## 1. Introduction

Clays are amongst the most abundant minerals at the Earth's surface and their impact on global trace element cycling stems from their ability to accumulate a range of trace elements, with the magnitude of adsorption being directly tied to their high surface charge and surface area (Landry et al., 2009; Sposito et al., 1999; Tournassat et al., 2004, 2016). Previous studies have shown that the surface charge of clay mineral (e.g., kaolinite, illite, and montmorillonite) varies with the ionic strength and pH of the background electrolyte solution (Bradbury & Baeyens, 2002, 2009; Gu & Evans, 2007; Hao et al., 2018; Hao, Flynn, et al., 2019; Liu et al., 2018; Sahai & Sverjensky, 1997; Sverjensky & Sahai, 1996). Accordingly, as clay-bearing particles are transported from land to the oceans, the change in aqueous conditions from freshwater and slightly acidic (pH = 6, ionic strength = 0.01 M) to saline and alkaline (pH = 8, ionic strength = 0.56–0.7 M) influences clay mineral surface properties, and ultimately affects the speciation and degree of adsorption of trace metals on clay mineral surfaces. For instance, previous studies demonstrated that an increase in solution ionic strength can attenuate the net negative electrostatic field at kaolinite, illite, and montmorillonite surfaces, decreasing cation adsorption and increasing anion adsorption (Hao et al., 2018, 2020; Hao, Flynn, et al., 2019). Conversely, the increase in pH from freshwater to marine conditions promotes the deprotonation of clay surface functional groups, generating additional negative charge which facilitates cation adsorption but inhibits anion adsorption.

Clay minerals that have experienced acid exposure (e.g., during acid rock drainage) have higher surface areas than clays generated in the presence of circumneutral aqueous solutions, and thus display different surface properties and element affinities. For instance, Hao, Pudasainee, et al. (2019) showed significant increases in the surface areas of clay minerals (kaolinite, illite, and montmorillonite) after exposure to

acidic solutions (pH  $\sim$  0–4), as well as decreased cadmium (Cd) adsorption. Similarly, Jeon and Nam (2019) showed that acidic treatment can decrease the surface functional group density and the proton binding constants of montmorillonite. Other variations in aqueous conditions, such as pH and ionic strength, can also impact the speciation of trace elements and the surface charge of clays, and thus control the affinity of trace elements to clays. For example, Hao et al. (2020) measured decreased Cd adsorption to illite and montmorillonite in solutions with increasing both pH (6–8) and ionic strength (0.01–0.56 M), mimicking changes from freshwater to seawater aqueous conditions. Those authors subsequently hypothesized that metal desorption in marginal marine settings could liberate trace metals to seawater, impacting primary productivity.

The next step in assessing the Hao et al. (2020) hypothesis is to study the association of trace elements with clay minerals in naturally acidic environments. In this regard, terrestrial hydrothermal settings are suitable because vent effluents are commonly acidic and rich in an assortment of trace metals, while the acidic steam actively promotes the in-situ formation of clay minerals. Previous field studies conducted by Liu et al. (2009) and Alsina et al. (2014) explored arsenic (As) geochemistry in geyser fields of China and Chile, respectively, and showed that the majority of aqueous As is adsorbed onto solid particles, as opposed to being present as free ions; and that particle-bound As is a significant source of groundwater As. Morteani et al. (2014) studied trace element concentrations in water and mud at hot springs in the Cordillera and the Altiplano of Bolivia. While these studies emphasized the occurrence of specific trace elements in the mud samples on a local scale, the surface reactivity and chemical speciation of surface functional groups of minerals within mud samples remain poorly understood, especially during environmental pH variations. Clay minerals experience a variety of chemical conditions during downstream transport; therefore, developing a flexible model that predicts the reactivity of clay minerals toward metals with varying environmental conditions is critical to accurately determining metal speciation, adsorption, and transport.

Our study focused on the El Tatio Geyser Field (ETGF), which is located in the northern part of the Atacama Desert in Chile (Figure 1). Understanding clay-bound trace element partitioning is of particular import in the ETGF as high levels of geogenic As in runoff from the ETGF contribute to making As pollution a major issue for water utilization and a human health risk factor in Northern Chile (Leiva et al., 2014; Smith et al., 2012). Studies at the ETGF have included: (1) fluid characterization and gas composition to trace the source of the fluids (Tassi et al., 2009, 2010), (2) environmental partitioning and phase associations of As and Sb along El Tatio geyser outflows (Landrum et al., 2009) and in the regional watershed draining from the ETGF (Alsina et al., 2014), (3) sedimentary fingerprints of microbial activity (Fernandez-Turiel et al., 2005; Gong et al., 2019; Sanchez-Garcia et al., 2019; Wilmeth et al., 2020), and (4) hydraulic and physico-chemical properties (Munoz-Saez et al., 2016, 2018; Nicolau et al., 2014). In this study, we sampled different boiling mud pots in the ETGF to study the partitioning and distribution of trace elements in hot spring muds and their speciation on clay mineral surface functional groups. Our goals are to (1) characterize the muds that naturally exist in the ETGF, (2) assess their control on trace element behavior, (3) determine the amount of trace elements that are weakly bound to clay mineral surfaces, and (4) predict the potential for trace element release when the muds encounter circumneutral pH waters and thus how muds affect water quality when transported downstream from the ETGF. Finally, we compare the experimental results with published geochemical data from the Rio Salado and Rio Loa to determine the potential contribution of clay-bound transport to metal/metalloid toxicity in northern Chile.

## 2. Geological Background

The ETGF is one of the largest and highest elevation (4,300 m) geothermal fields on Earth. The field area comprises an extremely arid plateau, the Northern Chilean Altiplano, extending from the Andes Mountains to the Pacific Ocean. The ETGF is one of several active geothermal fields in northern Chile (Tassi et al., 2010); it is geologically associated with the Altiplano-Puna Volcanic Complex (APVC), a large volcanic zone that extends north and south of the ETGF (De Silva, 1989; De Silva & Francis, 1991; De Silva et al., 1994; Lahsen & Trujillo, 1976).

The ETGF is the largest geyser field in the Southern Hemisphere, and the third-largest geyser field in the world, with over 80 active geysers, 30 perpetual spouters, as well as mud pots, warm springs, solfataras, and fumaroles (Glennon & Pfaff, 2003). ETGF water originates as rainwater and snowmelt in the Bolivian Andes

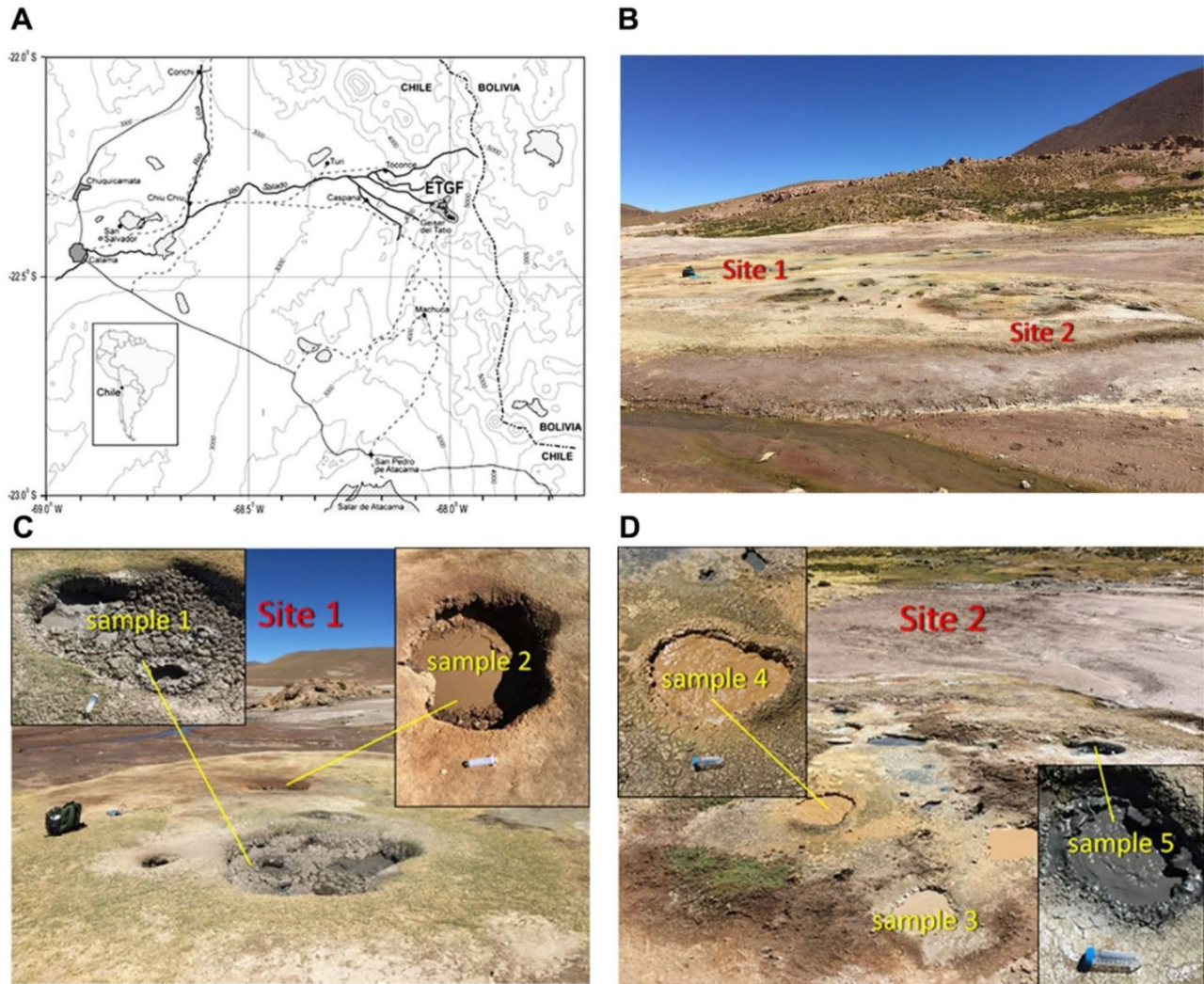


**Figure 1.** Map of field location with sampling sites (map modified from Landrum et al., 2009). (a) The El Tatio Geysers Field (ETGF). (b) Sampling sites of the five mud samples in the ETGF Upper basin (coordinates: 22°19′40.41″S, 68°0′23.81″W). (c) Site 1 where sample 1 and sample 2 were collected. Backpack for scale is roughly 60 cm tall. (d) Site 2 where samples 3, 4, and 5 were collected, standard 50 mL centrifuge tube (11.5 cm in length and 3.2 cm in width) for scale. ETGF, El Tatio Geysers Field.

15–20 km to the east-southeast, moves west through the deep subsurface and is heated up to 224°C by the Pastos Grandes and Cerro Gaucha caldera systems of the APVC just east of El Tatio (Cusicanqui et al., 1976; Giggenbach, 1978; Healy & Hochstein, 1973; Lahsen & Trujillo, 1976; Magaritz et al., 1990). Upon reaching the ETGF, groundwater becomes confined to two major aquifers: the Puripica and Salado ignimbrites and the Tucle dacite (De Silva, 1989; De Silva et al., 1994). Thermal features are located on north-south-oriented faults of the Tatio graben (Munoz-Saez et al., 2015, 2018).

Most ETGF geothermal features are clustered into areas known as the Upper, Middle, and Lower Geysers basins (Ellis, 1969; Glennon & Pfaff, 2003). The Upper Basin contains the highest number of geothermal features, including geothermal springs with low discharge, and spouting geysers forming well-developed silica sinter terraces along the high vertical relief N-NW margin. The Upper Basin's periphery hosts vegetated slopes with mud pots and fumaroles. The Middle Basin is a flat sinter plain with deep pools and fountain-type eruptions where individual features often have higher discharge than the Upper Basin springs. At higher elevation, the Middle Basin, known as Group M-III, also contains a cluster of active mud pots, springs, and solfataras, forming the main surface runoff that flows through the Middle Basin (Glennon &

**Table 1**  
*El Tatio Sampling Site Temperatures and pH (Sample Site Coordinates: 22°19'40.41"S, 68°0'23.81"W)*

	Temperature (°C)	pH	Water content of mud sample (%)	Color
Sample 1	54.2	3.55	82.55	Grey
Sample 2	40.1	4.87	82.39	Grey to brown
Sample 3	76.2	5.84	88.87	Brown
Sample 4	80.4	2.42	87.03	Brown
Sample 5	76.4	4.01	75.10	Grey

Pfaff, 2003). The Lower Basin lies along the banks of the Rio Salado, the headwaters of which are formed by geyser effluent from all three basins (Figure S1).

Two geochemically distinct types of circumneutral pH and moderately saline fluids emerge from geysers and springs at El Tatio: (i) deeply sourced, magma-heated water of Na-Cl-type, and (ii) meteoric and surface-runoff steam-heated in the shallow subsurface which contains sulfate (Cortecci et al., 2005). The deep, magmatically derived Na-Cl-type geyser waters are rich in As, B, Cs, and Li (Cortecci et al., 2005), and contain the world's highest naturally occurring As and Sb concentrations found in surface waters (0.3–0.6 mmol/L and 10–20 μmol/L, respectively, see Landrum et al., 2009), but extremely low dissolved inorganic carbon (0.1–0.5 mmol C/l, mainly as HCO<sub>3</sub><sup>-</sup>) (Ellis and Mahon, 1964, 1967; Landrum et al., 2009; Myers, 2015; Plenge et al., 2017). The pH of geyser waters at ETGF is circumneutral, ranging from 6.8 at most discharge points and increasing to 7.1 as waters cool along outflows (Landrum et al., 2009).

Mud pots, which tend to form along the margins of the hydrothermal field, adjacent to fresh volcanics and vegetation, are sulfate-rich and mostly fed by meteoric water and surface run-off (Cortecci et al., 2005). The contribution of this water into ETGF runoff is smaller than that of the geothermal Na-Cl-type water, but it possesses higher trace metal and dissolved gas concentrations (Cardenas & Engel, 2012; Cortecci et al., 2005; Tassi et al., 2010). In mud pots, locally high H<sub>2</sub>S gas (oxidizing to sulfuric acid in the aqueous phase), and CO<sub>2</sub> from plant roots in sandy, volcanically derived sediment contribute to high acidity and rapid mineral weathering, resulting in rapid clay formation.

The geyser fluids contain high concentrations of geogenic trace elements (e.g., As and Sb), and contribute to high levels of these elements in the Rio Loa, one of the main water sources for agriculture and human consumption in the Antofagasta region of Northern Chile (Landrum et al., 2009; Leiva et al., 2014). Runoff from the ETGF and other As-rich geothermal fields and mining sites combine to make As pollution a major issue for water utilization and a human health risk factor in Northern Chile (Leiva et al., 2014; Smith et al., 2012).

Unlike most natural waters where pH is buffered by the carbonate system, ETGF waters are strongly buffered by the arsenic acid system at the pK<sub>a2</sub> of arsenate, As(V) (H<sub>2</sub>AsO<sub>4</sub><sup>-</sup> ↔ HAsO<sub>4</sub><sup>2-</sup> + H<sup>+</sup>, pK<sub>a2</sub> = 6.94, see Landrum et al., 2009). Arsenic also buffers the redox: waters emerge with a 4:1 ratio of As(III): As(V), which is rapidly oxidized in the outflow channels (Engel et al., 2013; Landrum et al., 2009). Although As is a known toxin, microorganisms inhabiting ETGF streams and pools have adapted to tolerate, and in some cases, appear to benefit from the geochemical properties of As, making the ETGF microbial ecosystem unique (Engel et al., 2013; Escudero et al., 2013; Myers, 2015).

Most springs and geysers discharge water rich in amorphous silica near the local boiling point of 86°C. Opal-A precipitates as hydrothermal waters cool and evaporate, forming a variety of siliceous sinters at different temperatures and physical environments (Alsina et al., 2014; Fernandez-Turiel et al., 2005; Garcia-Valles et al., 2008; Landrum et al., 2009; Phoenix et al., 2006; Rodgers et al., 2002; Wilmeth et al., 2020). Thin iron oxide coatings are also observed on microbial mats and streamers in the moderate-to-high temperature regions along some geyser outflows (Engel et al., 2013; Landrum et al., 2009).

Most springs and geysers discharge water rich in amorphous silica near the local boiling point of 86°C. Opal-A precipitates as hydrothermal waters cool and evaporate, forming a variety of siliceous sinters at different temperatures and physical environments (Alsina et al., 2014; Fernandez-Turiel et al., 2005; Garcia-Valles et al., 2008; Landrum et al., 2009; Phoenix et al., 2006; Rodgers et al., 2002; Wilmeth et al., 2020). Thin iron oxide coatings are also observed on microbial mats and streamers in the moderate-to-high temperature regions along some geyser outflows (Engel et al., 2013; Landrum et al., 2009).

### 3. Methodology

#### 3.1. Sample Collection

Five different sites with a range of temperatures, pH values, and mud colors were chosen within an approximately 400 m<sup>2</sup> area of the ETGF Upper Basin on the southern edge of the Group U-VIII cluster (Figure 1 and Table 1). These features were mainly found along the margin of a vegetated, sandy slope, which comprises a range of shallow, steam-heated mud pots, interspersed with shallow, clear (non-mudpot) spring-fed pools and fumaroles. Solid mud samples were collected from the edges of the mud pots using a scalpel and then immediately placed into 20 mL high-density polyethylene (HDPE) vials that were filled to the top with mud

and sealed. Water samples were collected from the surface of the hot springs using a 20-mL syringe. The water samples were then filtered through 0.22  $\mu\text{m}$  nylon membranes (Agilent Captiva) into the same type of 20 mL HDPE vials. Three drops of 70% nitric acid were added to lower the solution pH to  $<3$  to prevent metals from either precipitating out of solution or adsorbing to the inner tube surfaces. The pH and temperature of the sites from which mud samples were collected were measured in situ (see data in Table 1) and the pH reading was temperature corrected. Once transported to the University of Alberta, the mud samples were dried in an oven at 90°C overnight to estimate water content.

### 3.2. Powder X-Ray Diffraction Analysis

Approximately 500 mg of each oven-dried (40°C) sample was ground by hand to  $<0.4$  mm using an agate mortar and pestle. Each sample was then ground in anhydrous ethanol using agate elements with a McCrone Micronizing Mill for 4 min. Samples were air-dried overnight and disaggregated using an agate mortar and pestle. A Ca-exchange was performed to stabilize the basal spacing of smectites to 15 Å following Bish et al. (2003) and using the method described by Mervine et al. (2018). The samples were suspended in 100 mL of 1 M  $\text{CaCl}_2 \cdot 2\text{H}_2\text{O}$  (Fisher Chemical, Certified ACS grade), sealed in Schott bottles, and agitated vigorously overnight. Following agitation, samples were gravity filtered through filter paper (Whatman no. 1). Samples were then rinsed 3 $\times$  with deionized water, dried overnight at room temperature, and disaggregated again with an agate mortar and pestle. Amorphous substances, including amorphous silica, are commonly undetectable in powder XRD patterns, even when present at abundances of several tens of wt% (Gualtieri, 2000). Because opal was tentatively identified in several samples using scanning electron microscopy (SEM) (see results), 10% (w/w) of synthetic  $\text{CaF}_2$  was added to each sample as an internal standard for quantification of this amorphous phase. Following the addition of  $\text{CaF}_2$ , each sample was ground for a further 40 s under anhydrous ethanol using stainless steel elements in a miniaturized McCrone milling assembly (using the design of Locock et al., 2012). Following McCrone milling, each powdered sample was mounted in a back-loaded cavity mount against a piece of frosted glass to minimize the preferred orientation of crystallites.

Diffraction patterns were collected using a Rigaku Ultima IV  $\theta$ - $\theta$  powder X-ray diffractometer (XRD) equipped with a D/Tex Ultra detector and a cobalt source that was operated at 38 kV and 38 mA. XRD patterns were collected from 5° to 80°  $2\theta$  using a step size of 0.02°  $2\theta$  at a rate of 2°  $2\theta$ /minute. Relative humidity was recorded at the beginning and end of each sample pattern collection and a humidifier was run during sample analysis to maintain relative humidity in the range of 20%–80% as per Bish et al. (2003). Mineral phase identification was conducted using the DIFFRAC.EVA XRD phase analysis software (Bruker) with reference to the International Center for Diffraction Data Powder Diffraction File 4+ database (ICDD PDF4+). Rietveld refinement (Bish & Howard, 1988; Hill & Howard, 1987; Rietveld, 1969) with XRD data was used to estimate mineral abundances with TOPAS 5 (Bruker). Fundamental parameters peak fitting (Cheary & Coelho, 1992) was used for all phases. The Partial Or No Known Crystal Structure (PONKCS; Scarlett & Madsen, 2006) method of structureless fitting was used to model the XRD patterns of kaolinite and montmorillonite to account for turbostratic stacking disorder. The use of Rietveld-compatible structureless fitting methods can result in overestimates of the structurally disordered phases for which they are used owing to overestimation of peak intensities at the expense of other phases with overlapping peaks (Turvey et al., 2018; Wilson et al., 2006). As such, when physically implausible peak intensities were observed for kaolinite or montmorillonite (in the late stages of refinement) we accepted refined parameters before convergence of the model.

### 3.3. Scanning Electron Microscopy

Dried, powdered samples were mounted on adhesive carbon films and sputtered with an nm-thick carbon layer to increase conductivity for SEM analyses. The samples were imaged on a Zeiss Sigma 300 VP-FESEM at an accelerating voltage of 10 kV operating in high-vacuum mode. Signals were collected with secondary electron (SE), back-scattered electron (BSE), and in-lens detectors. Elemental characterization of the mud samples was done using a Bruker energy dispersive X-ray spectroscopy (EDS) system.

### 3.4. Total Mud Digestions

Digestions using Teflon containers were conducted to assess the total elemental concentration in the collected mud samples. 0.1 g of each dried sample was weighed and then digested in 5 mL of 30% hydrogen peroxide (H<sub>2</sub>O<sub>2</sub>) and 5 mL of 70% nitric acid (HNO<sub>3</sub>, ACS certified, Thermo Fisher Scientific) at room temperature for 1 h and then at 120°C for an additional 1 h. Thereafter, 5 mL of hydrofluoric acid (HF) was added and the samples were then heated at 130°C for 3.5 h. The rest of the samples were further dissolved in 20 mL of 4.5% boric acid (H<sub>3</sub>BO<sub>3</sub>) at 130°C for 1 h to remove any remaining fluoride phases. Subsequently, the samples were filtered through 0.22 μm nylon membranes to remove residual organics and diluted 200 times in a mixture of 2% nitric acid and 0.5% hydrochloric acid (HCl) for concentration analysis.

### 3.5. Leaching Experiments

Mud samples were treated with acid and base to determine the weakly bound ions that were naturally adsorbed onto the solid surfaces. We conducted acid leaches to test the releasable elements at low pH while the alkaline leaches were designed to assess what elements desorb as the clay particles get transported downstream, where mixing with higher pH waters occurs. Specifically, 0.5 g of each sample was suspended in 50 mL of deionized water to make a 10 g/L suspension. The pH of the suspension was then adjusted to 2 by the addition of 70% HNO<sub>3</sub> to desorb ions into solution. The same treatment was performed at a pH of 12 using 5 M NaOH<sub>(aq)</sub> as an alkaline leach. In both cases, the suspension was then agitated on a tube rotator for 24 h to achieve equilibrium for surface adsorption/desorption reactions. Afterwards, the suspension was centrifuged at 17,000 g to separate the solid and liquid phase and the liquid phase was filtered through a 0.22 μm nylon membrane to collect the supernatant for trace elemental analysis.

### 3.6. Trace Elemental Concentration Analysis

The elemental concentration of total digested mud samples, the water samples, and the acid-base leaching samples were analyzed on an Agilent 8800 Triple Quadrupole Inductively Coupled Plasma Mass Spectrometry (ICP-MS) at the Environmental Geochemistry Lab (University of Alberta). The instrument was run in high matrix mode using argon (Ar) gas as the carrier and dilution gas. External calibration was done using a standard fluvial sediment (reference no. STSD-3) with obtained *R*<sup>2</sup> values >0.992. Internal standards, measurement modes, and detection limits are summarized in Table S1. Based on the trace elemental concentration, the concentration factor of trace elements on mud samples was calculated in a logarithm scale:

$$\log(\text{concentration factor for element } A) = \log\left(\frac{\text{concentration of element } A \text{ in mud}}{\text{concentration of element } A \text{ in water}}\right) \quad (1)$$

where *A* represents Al, U, Ce, Pb, Mo, P, Fe, Co, Zn, Si, Mg, Ba, Cr, Mn, As, K, Sr, Ca, Li, Na, and Cd.

### 3.7. Acid-Base Titrations

Acid-base titrations were performed on all five mud samples to determine their proton reactivities. Before titration, samples were leached with both acid and base (see above procedure) to remove trace elements adsorbed on the surfaces. The samples were rinsed with deionized water and centrifuged at 17,000 g to remove the liquid phase. The solid samples were then dried until a constant weight was attained. Potentiometric titrations of the dry mud samples were conducted using an automated continuous titrator (Metrohm Titrando 905). Before each titration, the pH electrode was calibrated using commercial pH buffers (Thermo Fisher Scientific; pH 4.0, 7.0, and 10.0). For each titration, 0.05 g of each mud was suspended into 50 mL of 0.01 M sodium nitrate (NaNO<sub>3</sub>) solution, and the suspension was then bubbled for 30 min with N<sub>2</sub>(g) to ensure the absence of CO<sub>2</sub>. During titrations, the experimental apparatus remained sealed and was continuously bubbled with N<sub>2</sub> to prevent CO<sub>2</sub> from entering the system. All mud samples were titrated over a pH range of 3.0–10.5; initially, a small volume of 0.1 M HNO<sub>3</sub> was added to bring pH to 3.0, and then 0.1 M sodium hydroxide (NaOH) solution was added incrementally to increase pH to 10.5. The volume of acid and base added, and the corresponding pH change was recorded at each titration step. The pH was considered stable and recorded only after an electrode stability of 12 mV/min was achieved.

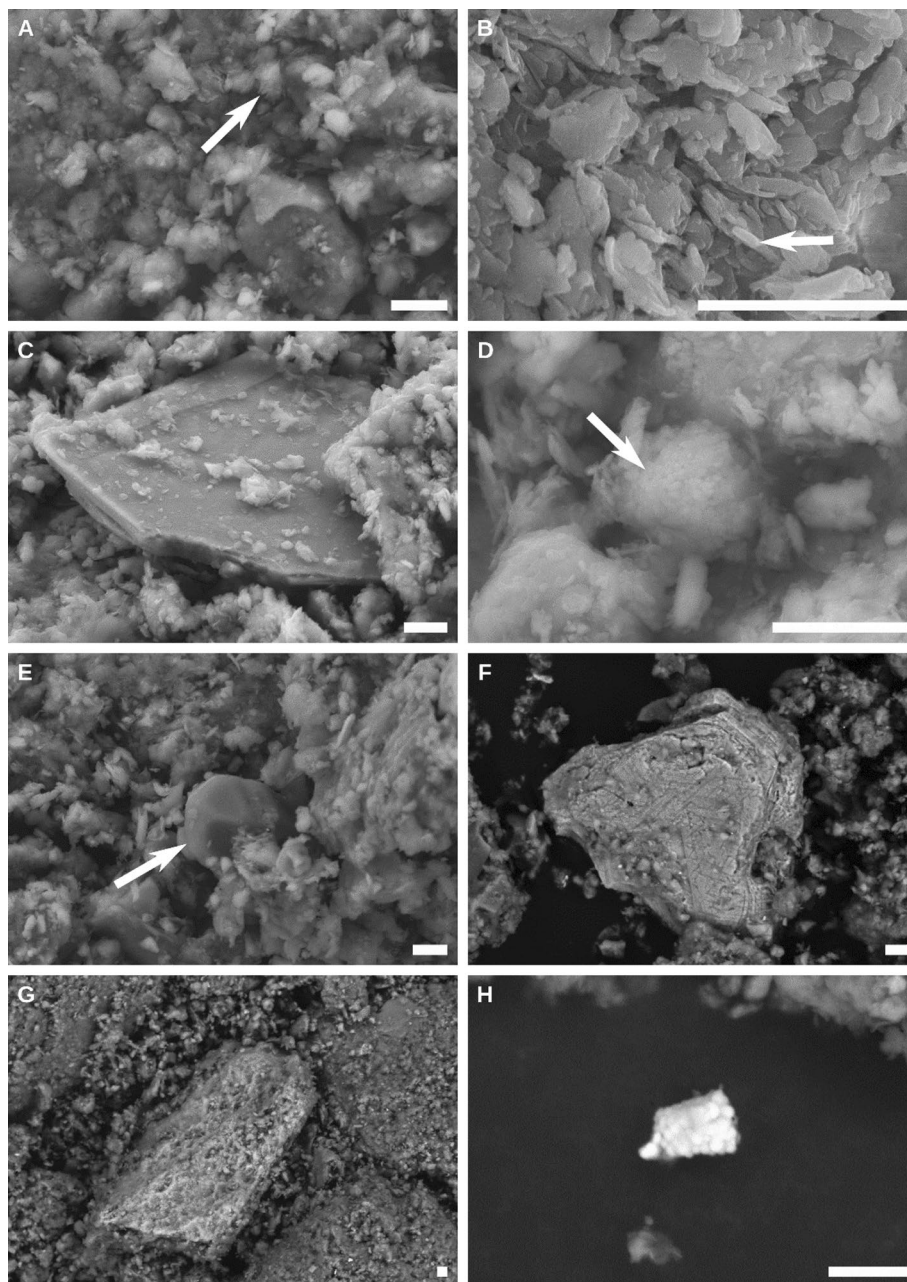


**Figure 2.** Scanning electron microscopy images of ETGF mud samples. (a), (b) Clay aggregates from sample 1 form the majority of the sample matrix and have 50–100 nm diameter flakes on their surfaces (marked by arrows). (c) A large, subhedral grain of a phyllosilicate mineral from sample 2. (d), (e) Subspherical SiO<sub>2</sub>-rich nodules (marked by arrows) from samples 1 and 2, respectively. The grain in panel (d) is possibly opal, whereas panel (e) likely depicts a detrital quartz grain. (f) Back-scattered electron image of a Fe-Ti oxide grain in sample 3. (g) Back-scattered electron image of a Fe-S-As phase from sample 5. (h) Back-scattered electron image of an As-Sb rich particle in sample 2. The white scale bars on the bottom right corners represent 2  $\mu\text{m}$ . ETGF, El Tatio Geyser Field.

## 4. Results

### 4.1. SEM Analyses

SEM imaging revealed that the mud samples appear generally similar; the majority of the matrix in each sample consists of a disordered mass of aggregates of anhedral clay mineral grains (Figure 2a). Once magnified, the aggregate surfaces appear broken up into  $\sim 100$  nm diameter plates and short acicular crystals

(Figure 2b). Occasionally, larger clay flakes, up to 100  $\mu\text{m}$  in diameter, were observed (Figure 2c, EDS result in Figure S2a).

Some differences between samples can be deduced in the distribution of  $\text{SiO}_2$  and Fe phases. In samples 1, 2, and 5, subspherical  $\text{SiO}_2$ -rich particles, 1–2  $\mu\text{m}$  in diameter, appear amongst the clay aggregates, displaying a blotchy surface (probably opal-A and/or detrital quartz, Figures 2d and 2e). Subhedral Fe and Ti-rich grains  $>10 \mu\text{m}$  in size were evident in samples 2 and 3 (Figure 2f), and a Fe-S-As phase in sample 5 (Figure 2g). No pyrite particles were visually detected in any sample, although submicrometer S-rich particles, bright under BSE mode but too small to reliably analyze via EDS, were found in sample 5 (likely either orpiment or elemental sulfur, Figure S2e). Finally, minor As-Sb rich phases were seen in samples 2 and 5, similar to a phase described by Mountain et al. (2001) (Figure 2h).

#### 4.2. Powder X-Ray Diffraction Analysis

The Rietveld refinement plot for mud sample 4 is presented in Figure 3a as an example of the XRD pattern for the mud samples; the remaining plots are given in Figure S3. Refined mineral abundances for the five mud samples are provided in Figure 3b. The minerals identified (in order of most to least abundant) are kaolinite [ $\text{Al}_2\text{Si}_2\text{O}_5(\text{OH})_4$ ], montmorillonite [ $(\text{Na,Ca})_{0.33}(\text{Al,Mg})_2(\text{Si}_4\text{O}_{10})(\text{OH})_2 \cdot n\text{H}_2\text{O}$ ], feldspar [sanidine,  $\text{K}(\text{Al-Si}_3\text{O}_8)$ ], muscovite [ $\text{KAl}_2(\text{AlSi}_3\text{O}_{10})(\text{OH})_2$ ] and silica (both cristobalite and quartz). The montmorillonite 001 peak at  $\sim 6.8^\circ 2\theta$  ( $\text{CoK}\alpha$ ) has a  $d$ -spacing of  $\sim 15 \text{ \AA}$  and the kaolinite 001 peak at  $\sim 14.3^\circ 2\theta$  has a  $d$ -spacing of  $\sim 7.1 \text{ \AA}$ . All five samples consisted primarily of clay minerals, with  $>50 \text{ wt\%}$  made up of the dioctahedral clay minerals kaolinite and montmorillonite, except for sample three in which these two minerals made up only 38.5 wt% of the crystalline mass. Sanidine is a major non-clay mineral that was observed in all five mud samples, accounting for between 22.6 and 34.0 wt% of the total mineral content (Table S2). Muscovite was found at its highest concentrations in sample 3 (up to 24.2 wt%). Approximately 3.2 wt% of quartz was detected in mud sample 2, whereas no quartz was detected in the rest of the samples. Despite micrometer-scale spheres of silica being observed in SEM micrographs (Figures 2d and 2e), opal was not present at sufficiently high abundance in any of the five samples to permit its quantification using Rietveld refinement with XRD data. As such, the internal standard ( $\text{CaF}_2$ ) added to the samples could not be employed for this purpose, and its abundance was normalized out of modal mineralogy results. Many other trace phases ( $<<1 \text{ wt\%}$ ) observed during SEM imaging were below detection for our XRD analysis, including Fe-oxide and As-Sb-bearing phases.

#### 4.3. Elemental Composition of Mud and Water Samples

The major elements in the five mud samples are silicon (Si) and aluminum (Al), with concentrations ranging from 19 to 24 wt% and 8 to 10 wt%, respectively (Table S3). The next most abundant elements are iron (Fe; 2.8–7.9 wt%), potassium (K; 2.3–4.0 wt%), sodium (Na; 0.1–1.7 wt%), magnesium (Mg; 0.2–0.7 wt%), and calcium (Ca; 0.2–0.8 wt%). Trace elements with concentrations in excess of 100  $\mu\text{g/g}$  are arsenic (As; 136.2–4,231.8  $\mu\text{g/g}$ ), phosphorous (P; 107.5–720.2  $\mu\text{g/g}$ ), barium (Ba; 285.2–524.6  $\mu\text{g/g}$ ), lithium (Li; 46.4–232.3  $\mu\text{g/g}$ ), manganese (Mn; 125.5–227.6  $\mu\text{g/g}$ ), strontium (Sr; 102.9–191.5  $\mu\text{g/g}$ ), and zinc (Zn; 65.6–199.6  $\mu\text{g/g}$ ). The concentrations of cadmium (Cd), cerium (Ce), cobalt (Co), chromium (Cr), molybdenum (Mo), lead (Pb), and uranium (U) are all below 100  $\mu\text{g/g}$ .

Among the water samples, the pH varies from 2.42 to 5.84. The dominant ion is Na with concentrations ranging from 33.54 to 1,126.45 mg/L. It is followed by K (20.6–136.9 mg/L), Ca (7.9–95.0 mg/L), Si (65.2–113.9 mg/L), As (0.1–10.9 mg/L), Fe (1.0–4.1 mg/L), Mg (0.4–4.0 mg/L), and Sr (0.09–1.6 mg/L). All other elements have concentrations below 1.0 mg/L, with Ce, Co, Mo, Pb, and U below 1  $\mu\text{g/L}$ . This indicates that they are primarily associated with the solid phase muds, while only a small fraction is dissolved in the aqueous phase.

Mud sample 1 has the highest Na, Li, Zn, As, and Ce concentrations amongst the five sites sampled. The concentrations of Li, Na, and As in water sample 1 are also the highest, indicating the fluid source of mud pot one is enriched in both Li and As. The relatively lower concentrations of Zn and Ce in water sample 1 compared to other water samples could be attributed to the adsorption of these elements onto the surfaces of mud sample 1. The concentrations of K, Mn, Fe, and Pb in mud sample 1 are the lowest among the five

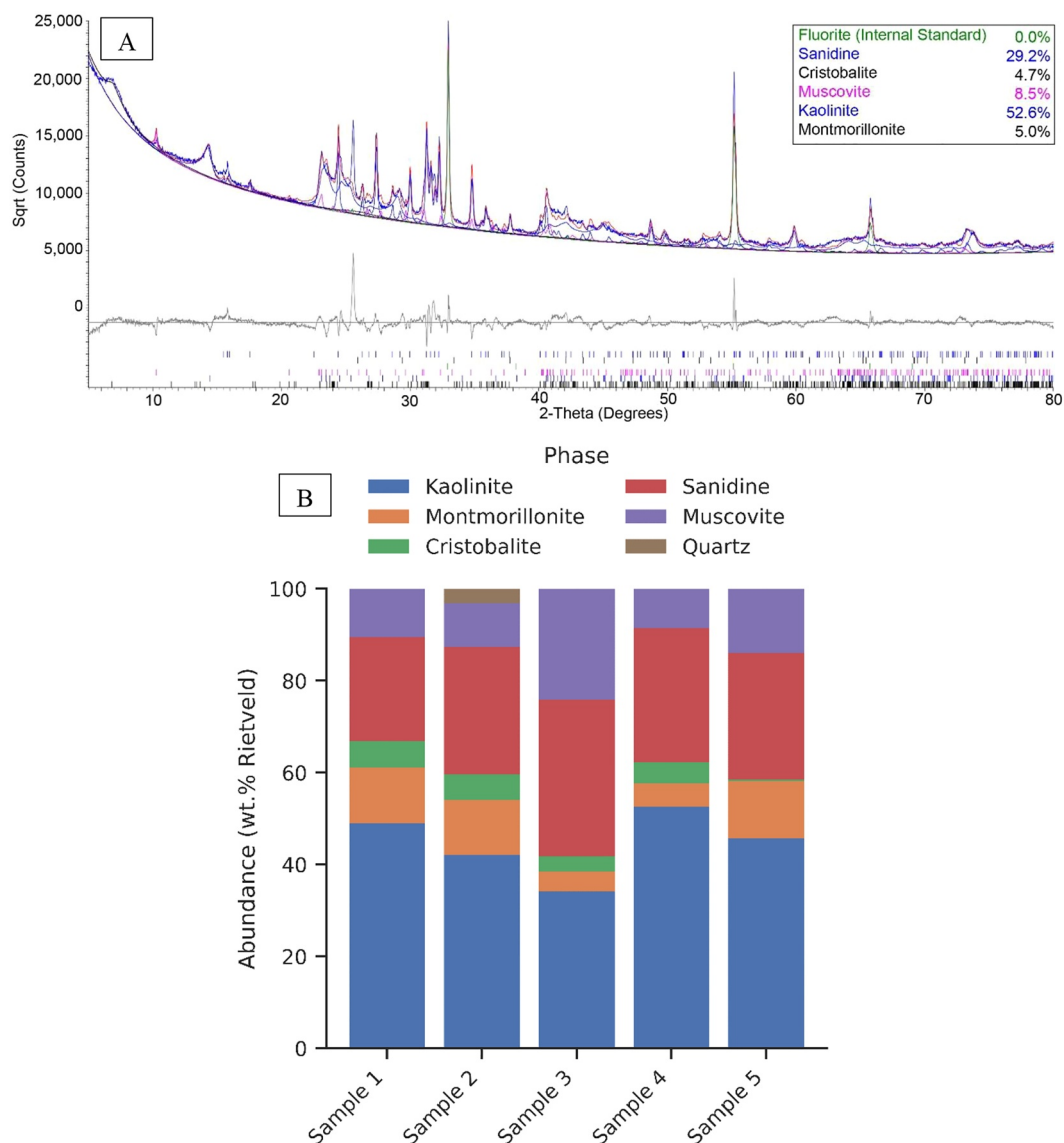


**Figure 3.** (a) Rietveld refinement plot for ETGF mud sample 4. Refined mineral abundances are given as wt% values. (b) Refined mineral abundances (wt%) for the five mud samples. ETGF, El Tatio Geyser Field.

mud samples, and their corresponding concentrations in water sample 1 are relatively high (compared to other water samples), indicative of the low affinity of these elements to mud surfaces.

The concentrations of Ca, Sr, Ba, and Pb are the highest in mud sample 2 amongst all five mud samples and none of these elements show the highest concentration in water sample 2, which is because of their high affinity to the solid phase. Intriguingly, sample 2 has the lowest P, As and Mo concentrations in mud, but the highest P and relatively high As and Mo concentrations in water, indicating the low affinity of anions for mud sample 2.

Mud sample 3 was collected from the highest pH pool, and correspondingly, it has the highest Mg, Cd, U, and relatively high Fe concentrations. The concentrations of Mg, Cd, U, and Fe in water sample 3 are the lowest, likely due to the hydrolysis and precipitation or adsorption of these elements on solid surfaces.

Mud sample 4 was collected from the lowest pH mud pool, and it has relatively high concentrations of anions such as P and As, but the lowest cation concentrations, including Li, Na, Mg, Ca, Co, Sr, Cd, and Ce.

**Table 2**  
Percentage of Each Element That is Desorbed From the El Tatio Mud Samples During Acid/Base Treatment

	Acid treatment (%)					Base treatment (%)				
	Sample 1	Sample 2	Sample 3	Sample 4	Sample 5	Sample 1	Sample 2	Sample 3	Sample 4	Sample 5
Li	85.70	42.49	50.78	bld	bld	68.80	bld	40.60	bld	bld
Na	100	42.09	77.72	100	97.24	na	na	na	na	na
Mg	bld	3.24	2.35	6.30	2.55	bld	bld	bld	bld	bld
Al	bld	3.03	bld	bld	bld	0.09	0.07	0.19	1.30	1.15
Si	0.57	0.73	0.87	0.61	0.33	1.30	0.93	1.46	2.69	1.41
K	18.08	4.30	5.96	bld	2.62	11.63	bld	4.37	bld	1.96
P	7.38	28.64	33.60	8.80	35.90	37.50	31.21	22.85	31.50	51.06
Ca	61.45	29.20	46.63	97.19	64.80	9.62	3.01	0.82	11.72	2.43
Cr	bld	11.29	bld	bld	bld	bld	bld	bld	bld	bld
Mn	12.33	11.01	22.47	17.09	9.00	bld	2.18	bld	bld	bld
Fe	3.99	1.61	1.38	0.17	2.28	0.04	0.10	0.21	0.52	0.87
Co	19.42	17.02	9.45	16.88	100	bld	6.35	5.86	15.70	4.61
Zn	bld	bld	bld	bld	bld	bld	8.44	bld	bld	21.68
Sr	31.11	17.29	24.21	34.36	24.94	2.51	1.69	bld	bld	0.42
As	41.62	53.47	25.89	0.49	10.15	77.88	48.24	25.82	18.40	18.60
Mo	71.66	100	96.14	19.12	6.11	22.18	30.01	39.89	16.99	22.30
Cd	100	96.16	6.03	bld	38.78	22.79	38.76	bld	bld	bld
Ba	2.14	3.15	2.38	15.34	2.47	bld	bld	bld	bld	bld
Ce	0.20	0.15	0.98	0.70	0.10	bld	6.54	bld	0.89	0.44
Pb	4.28	4.29	5.58	3.21	7.95	1.28	1.27	1.45	2.02	1.72
U	2.16	5.74	4.14	4.61	4.37	bld	0.37	4.55	2.07	1.19

Note. “bld” means below detection limit; “na” means not applicable (because of the external addition of Na during base treatment); percentage is calculated using Equation 1.

This is due to the fact that low pH conditions facilitate anion adsorption but inhibit cation adsorption onto clay surfaces.

Mud sample 5 has the highest Cr, Co, and Mo concentrations but the lowest Zn and Ba concentrations. Coupled with the relatively low Zn and Ba concentrations in water sample 5, this may indicate that the Zn and Ba reservoirs in mud pool 5 are relatively low compared to other mud pools.

#### 4.4. Acid-Base Leaching Results

During acid-base leaching, the elemental concentrations in the supernatants were measured and converted into  $\mu\text{g}$  of element per g of mud sample based on the mud-liquid ratio (Table S4). We applied the following equation to calculate the percentage of weakly bound elements in mud samples:

$$\% \text{ of weakly bound elements} = \frac{\mu\text{g of element released per g of mud sample during acid - base leaching}}{\mu\text{g of element per g of mud sample prior to leaching}} * 100\% \quad (2)$$

where the elements calculated include Al, U, Ce, Pb, Mo, P, Fe, Co, Zn, Si, Mg, Ba, Cr, Mn, As, K, Sr, Ca, Li, Na, and Cd. The results are listed in Table 2. Amongst the elements studied, Li, Na, and Ca are the most prone to leaching under acidic conditions. Almost half of the As was released under acidic conditions for samples 1 and 2, while 25.9% and 10.2% were released for samples 3 and 5, respectively, and only 0.5% for sample 4. Cadmium in samples 1 and 2 was desorbed almost fully in acid but only 6.0%, 0% (below detection

limit), and 38.78% were desorbed in samples 3, 4, 5, respectively. Similarly, over 50% of Ca in samples 1, 4, and 5 (61.5%, 97.2%, and 64.8%, respectively) was desorbed under acidic treatment, but only 29.2%, 46.6% for samples 2 and 3, respectively. Molybdenum in samples 1, 2, and 3 was susceptible to acidic leaching (71.7%, 100%, and 96.1%, respectively), while in samples 4, 5, the percentage was only 19.1% and 6.1%. The release of P at low pH was relatively minor with only 7.4%, 28.6%, 33.6%, 8.8%, and 35.9% released for samples 1–5.

The alkaline treatment released 77.9% of the As from sample 1 and 48.2% from sample 2, compared to 25.8%, 18.4%, and 18.6% from samples 3, 4, and 5, respectively. Cadmium release under alkaline treatment ranged from 22.8% to 38.8% for the five samples which were lower than acidic treatment. The same behavior was observed for Ca with alkaline treatment, only releasing less than 10% of Ca from the mud samples (except 11.7% for sample 4). The release of Mo for all five studied samples ranged from 17.0% to 39.9% under high pH conditions. Phosphorus is more easily released under alkaline conditions with the pH 12 solution releasing 51.1% of the P in sample 5, and 37.5%, 31.2%, 22.9%, and 31.5% in samples 1–4, respectively.

The other elements (U, Pb, Ce, Fe, Si, Al, and Mg) were all rather immobile (less than 10% desorption) under both acid and base leaching, suggesting they are associated strongly with the solid phase, possibly forming inner-sphere complexes or residing within the crystal structures of minerals rather than being adsorbed to mineral surfaces.

## 5. Discussion

### 5.1. The Influence of Petrology and the Local Environment on the Mineralogy of the Mud Samples

The El Tatio geothermal field is situated in the volcanically active, Quaternary-age Altiplano-Puñá Volcanic Complex of the Central Volcanic Zone in northern Chile. The major host rock of the Tatio basin is primarily composed of ~1-km-thick ignimbrites, tuffs, and lavas with dacitic composition (De Silva et al., 1994; Healy, 1973; Lahsen, 1988; Lahsen & Trujillo, 1976). This is consistent with the observed occurrence of felsic volcanic minerals such as sanidine, muscovite, and cristobalite in mud pools sampled for this study, and this composition can be considered representative of mud pools found throughout the Upper and Middle (Group M-III) Basins of the geothermal field. The main geothermal field is covered by a relatively thin (1-to-tens-of-meters-thick) silica sinter platform formed during recent geothermal activity (Munoz-Saez et al., 2016; Nicolau et al., 2014; Wilmeth et al., 2020), overlying the deep dacitic ignimbrite aquifer (Cusicanqui et al., 1976; Tassi et al., 2010). Although the precise source of As in the geothermal fluids is unknown and it is possible that As is derived from magmatic fluid according to previous studies (e.g., Allard et al., 2000; Edmonds et al., 2018; Mather et al., 2012), As:Cl ratios in fluids are conservative, indicating steady leaching from the host rock at high temperatures in the aquifer (Landrum et al., 2009). This process may be analogous to the high degree of As leaching observed in natural and experimental samples examined during this study. These results shed light on the importance of dacitic volcanic deposits, and the process of leaching as a regional source of As contamination.

### 5.2. Concentration Factors and Inherent Element Behavior

The concentration factor of trace elements in mud samples (logarithm of concentration in mud/concentration in water) is presented in Figure 4. All elements are highly enriched in muds, with a log scale concentration factor of >1 (indicating >10 times enrichment in the mud phase relative to the liquid phase) for most elements. Specifically, the concentration factors of Ce, Al, U, and Fe are higher than 4 (>10,000 times enrichment) for most of the samples, and low concentration factors are observed for Na and Li (lower than 1). Elements, such as Pb, P, As, and Mo, have concentration factors around 2–4 (100–10,000 times enrichment). Except for Al (which is a structural element in clays), Ce is highly enriched in the mud phase due to its irreversible adsorption onto clay minerals and the formation of 12 inner-sphere covalent bonds with O (Fuller et al., 2015). Ferric iron usually precipitates on the surfaces of mud samples and forms ferric hydroxides containing As and S (Figure S2e). Uranium adsorption onto clay minerals is pH-dependent, being higher at neutral to high pH but lower at acidic pH (Bachmaf & Merkel, 2011). This adsorption behavior explains the lower concentration factor in sample 4 (collected at pH 2.42, Table 1) compared to samples 1, 2, 3, and 5 (collected at pH from 3.55 to 5.84, Table 1). Monovalent ions, such as Li<sup>+</sup> and Na<sup>+</sup>, are exchangeable

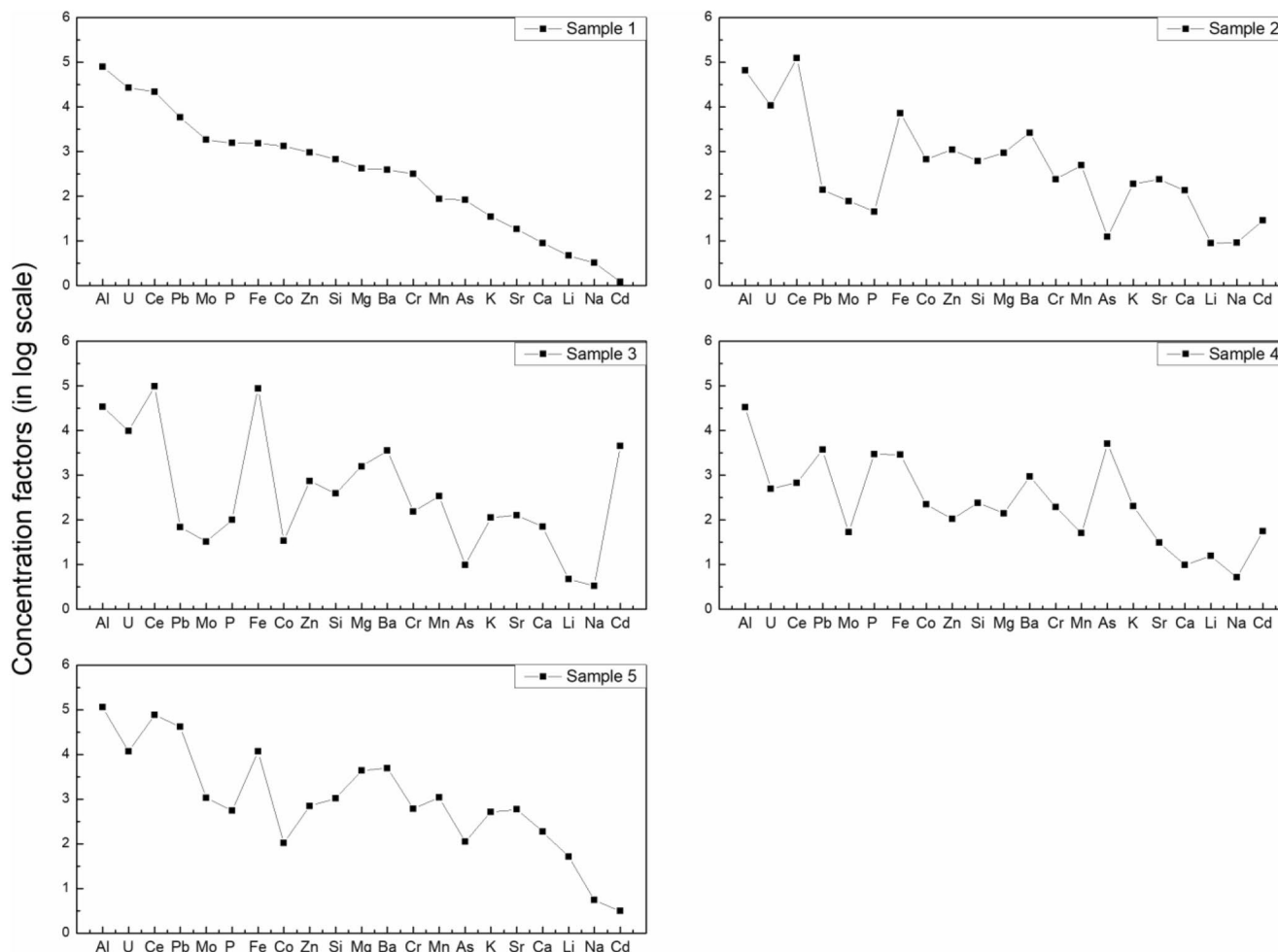


**Figure 4.** Relative distribution of elements between the clay and water phases (higher values mean the element is more closely bound to the solid phase). The order of elements in the x-axis is based on the decreasing trend in sample 1.

on clay interlayers, and show relatively lower concentration factors in mud samples. By comparison,  $K^+$  is relatively enriched compared to  $Li^+$  and  $Na^+$  because it is relatively stable in muscovite interlayers and, therefore, resistant to exchange (Scott & Smith, 1966).

Elemental concentration factors in each mud sample were compared with the average of all five samples (concentration factor of each element in every mud sample/average concentration factor of the element in all five samples; Figure 5). Mud sample 1 has high concentration factors for U, Mo, P, and Co, but low concentration factors for Mg, Ba, Mn, K, Sr, Ca, Li, Na, and Cd. Similarly, sample 4 has high concentration factors for P and As, but low concentration factors for U, Ce, Mo, Zn, Mg, Mn, Sr, and Ca. Both mud samples show high affinities to anionic elements such as P and As, but low affinities to cationic elements such as Mg, Mn, Sr, and Ca. This behavior can be attributed to the fact that samples 1 and 4 were collected at low pH pools (pH = 3.55 and 2.42, respectively), and at low pH conditions clay surfaces are protonated, which repulses cations but attracts anions (Lützenkirchen et al., 2012; Sposito et al., 1999). By contrast, samples 2 and 3 were collected at relatively higher pH pools (pH = 4.87 and 5.84, respectively), and both samples have low concentration factors for anionic elements such as Mo, P, and As, but high concentration factors for cationic elements such as Cd, Na, and Ca. These trends support a pH-control mechanism, mimicking the natural trend of pH increase from source-to-sink, for trace elemental enrichment. Sample 5 was collected at a mud pool with pH = 4.01, and has high concentration factors for Pb, Mo, Mg, Mn, K, Sr, Ca, and Li, but low concentration factors for Co and Cd.

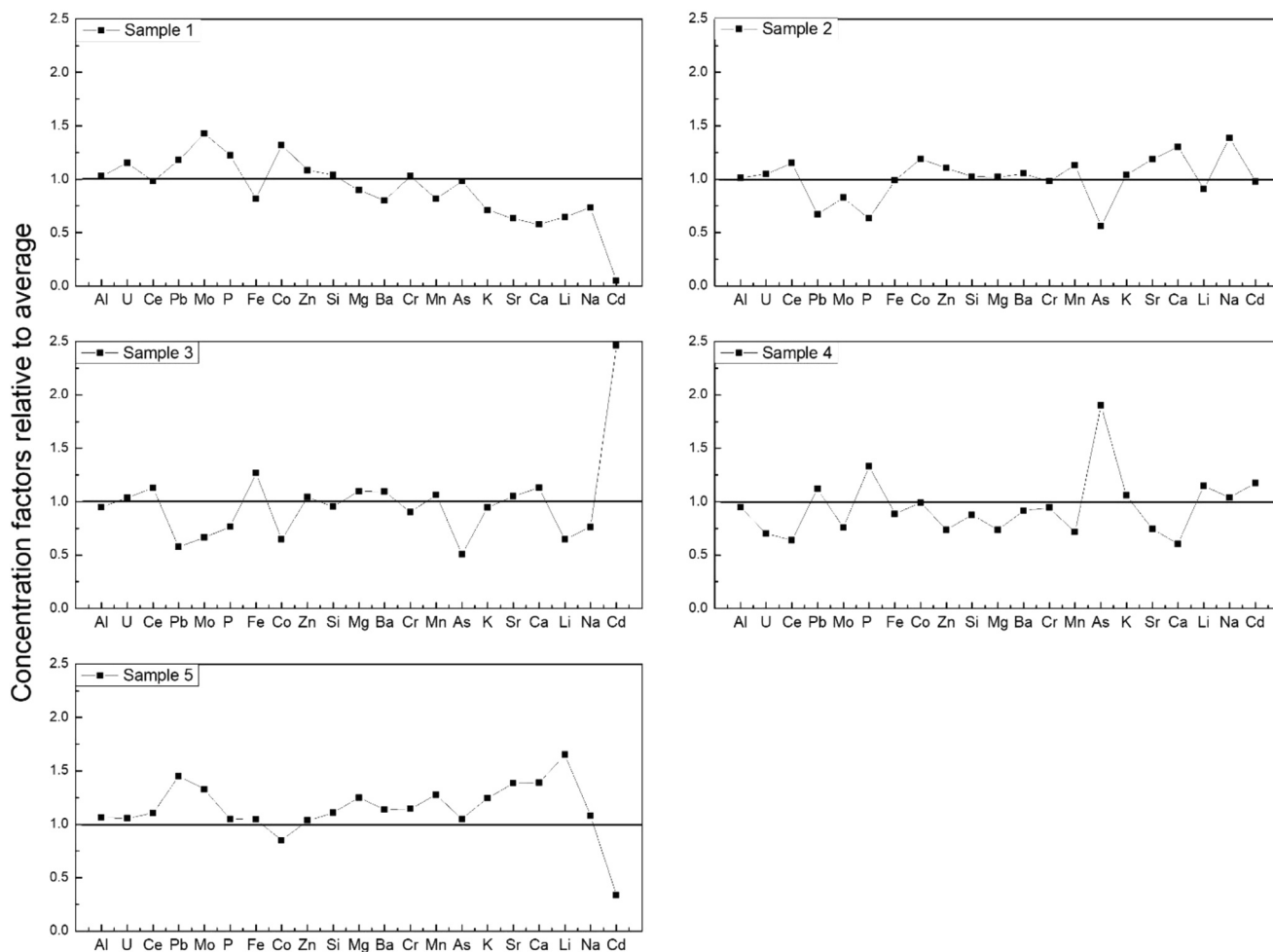
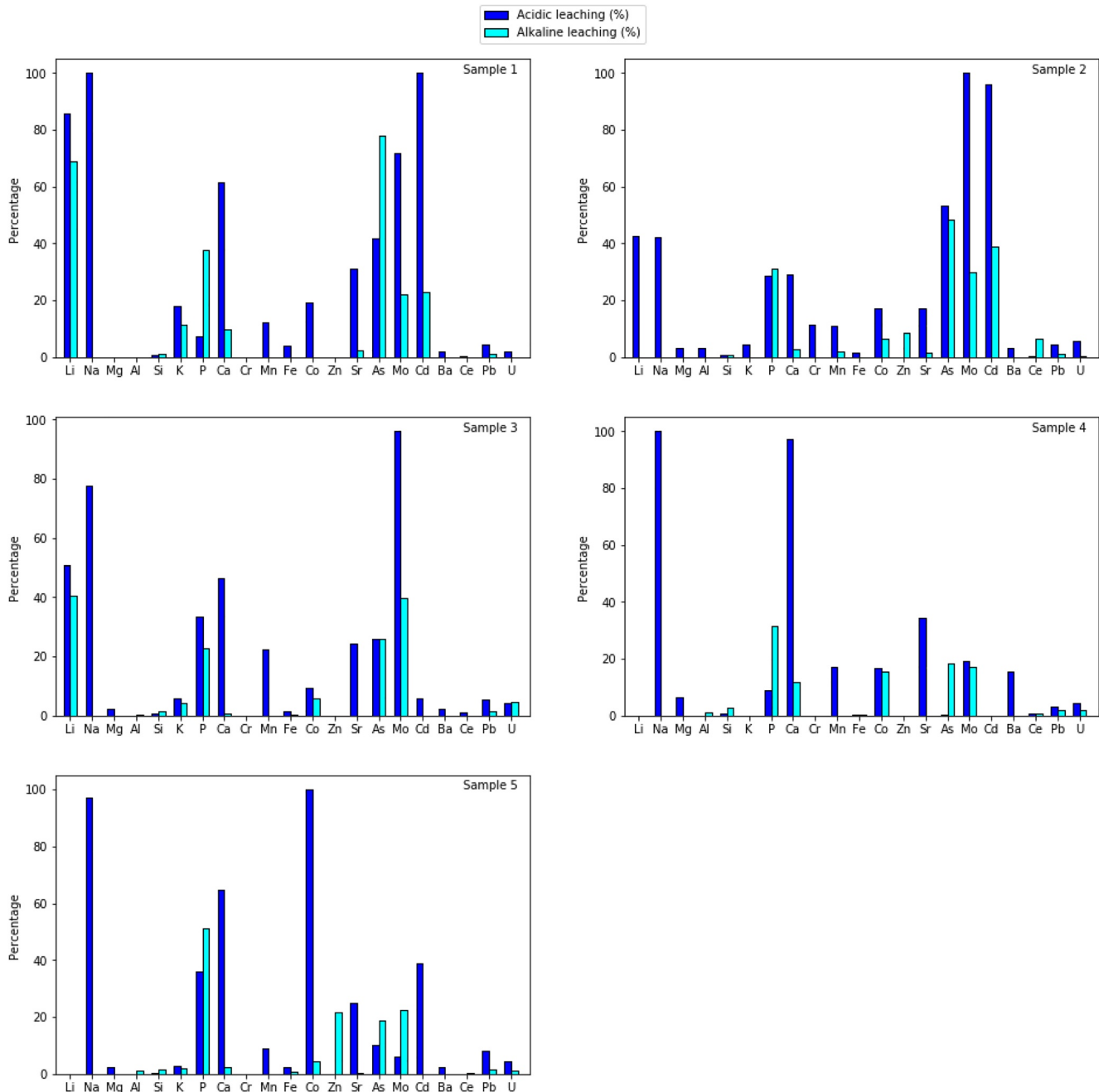


Figure 5. Concentration factors of each element relative to the average concentration factor of the element.

### 5.3. Element Mobility During Experimental pH Change: Mimicking Downstream Transport

The acid-base leaching experiments largely confirm the findings above in that solution pH ultimately dictates elemental sorption to clay minerals. Indeed, a large fraction of the elements analyzed are prone to dissociate from mud in response to environmental pH variation, especially P, Ca, Co, Sr, As, Mo, and Cd. The differences in mobility can be explained through adsorption, precipitation, and partitioning/incorporation of elements in the mud samples. For example, Cd only desorbs from mud surfaces under more acidic conditions (acidic treatment releases more Cd compared to alkaline treatment; Table 2 and Figure 6), which agrees with our previous findings that Cd primarily forms outer-sphere complexes under acidic conditions, but inner-sphere complexes under alkaline conditions (Hao et al., 2020). Similarly, Ca is mostly an exchange cation at clay interlayers which can be replaced and released back into solution at low pH conditions, but precipitates on clay surfaces as calcium hydroxide (which is controlled by Ca cation hydrolysis) at high pH conditions. Previous studies showed that the adsorption of Co and Sr onto kaolinite increases with solution pH (Angove et al., 1998; Jeong, 2001), which explains why Co and Sr desorbed more under acidic treatment than alkaline treatment in our leaching experiments (Table 2 and Figure 6).

By comparison, P (in the form of aqueous phosphate species such as  $\text{PO}_4^{3-}$ ,  $\text{HPO}_4^{2-}$ , and  $\text{H}_2\text{PO}_4^-$ ) adsorbs on clay minerals at low pH (Gérard, 2016), and at high pH, the release of P from the mud surfaces is expected. Such adsorption behavior on clay minerals can also be observed for anions such as As (Goldberg, 2002), which corresponds to our experimental results where As is preferentially released under alkaline conditions compared to acidic conditions (except for sample 2). It is also worth noting that the adsorption of Mo onto



**Figure 6.** The percentage of trace elements released during the acid and base leaching experiments for the mud samples. Blue bars represent acid leaching; cyan bars represent alkaline leaching.

clay minerals decreases with increasing pH (Goldberg et al., 1996), yet our experimental results show only 30%–40% of Mo released for samples 2 and 3 under alkaline treatment but almost 100% of Mo release under acidic treatment (Figure 6). This could possibly be attributed to the dissolution of minor Mo minerals (which are below the detection limit of XRD) under acidic conditions.

The affinity of trace elements onto clay surfaces can also be explained by the surface charge properties of the minerals. For example, the  $pH_{PZC}$  of kaolinite and illite determined by zeta potential are lower than 3 (e.g., Kosmulski, 2011; Liu et al., 2018). However, the  $pH_{PZNPC}$ , determined by acid-base titration, indicates that the surface functional groups of kaolinite, illite, and montmorillonite are primarily protonated below

pH 5.6, leading to a net positive surface proton charge for functional groups at those conditions. These functional groups become progressively deprotonated with increasing pH (Hao et al., 2018), increasing the proportion of negatively charged surface functional groups and leading to the repulsion of anions but the attraction of cations.

In contrast with the above elements, Cr and U are immobile when subject to environmental pH variations. This is probably because the interaction between Cr and clay minerals is through strong inner-sphere bonding. Our unpublished experimental study of Cr binding onto clay minerals using Extended X-ray Absorption Fine Structure (EXAFS) spectroscopy analysis showed that Cr adsorption could lead to isomorphic substitution of Al with Cr on octahedral sheets at the surfaces of clay minerals. This suggests that most of the Cr in the mud samples is structurally bound (partitioning) into the clay mineral lattice. Similarly, in all 5 mud samples, U is resistant to being released from clay mineral surfaces over the tested range of pH (Table 2 and Figure 6), which is possibly due to its inner-sphere complexation onto clay minerals (Catalano & Brown, 2005; Krepelova et al., 2008; Schlegel & Descostes, 2009). Another example of a structurally bound element is Ce. Once adsorbed onto clay surfaces, Ce is incorporated into clay interlayers (especially illite; see discussion in Section 5.2) and forms strong bonds between clay sheets. As a consequence, Ce is resistant to mobilization during acid-base leaching. Our results showed that Pb is relatively immobile under both acidic and alkaline conditions (less than 8% of Pb is released under acidic conditions for all five samples, and less than 3% under alkaline conditions), which indicates the possibility of incorporation of Pb into the structures of mud minerals.

While we highlight the importance of clay minerals in assembling trace elements from mud pools, it is also worth noting that other minerals in the mud samples (e.g., quartz, cristobalite, sanidine, and muscovite) may exert some control on trace elemental behavior. For example, acidic leaching of muscovite in stone coal can release K, Al, and V, with K being the most easily leached element (Xue et al., 2015). Similarly, acidic treatment of sanidine grains from a trachyte tuff in Volkesfeld, Germany shows that acid leaching could lead to the formation of a layer depleted in Na, K, Al on the surface of sanidine crystals (Adriaens et al., 1999). However, we emphasize the role of clay minerals because they constitute the major minerals in mud pools and by their high surface area and surface charge properties, they can be expected to be more critical in controlling trace elemental behavior than other minerals.

#### 5.4. Surface Complexation Modeling of the ETGF Mud Samples

Surface complexation modeling (SCM) was used to model the protonation-deprotonation behavior of functional groups on the surfaces of minerals in mud samples as a function of solution pH. Since the mud samples are mostly composed of clay minerals, we applied the same model for protonation and deprotonation surface reactions as used in previous clay studies (Barbier et al., 2000; Hao et al., 2018; Hao, Flynn, et al., 2019; Ikhsan et al., 2005; Lackovic et al., 2003; Peacock & Sherman, 2005). The following surface complexation reactions and corresponding mass action equations were used:



$$K = \frac{[\equiv \text{LH}] \cdot \alpha_{\text{Na}^+}}{[\equiv \text{LNa}] \cdot \alpha_{\text{H}^+}} \quad (3)$$



$$K_{a^-} = \frac{[\equiv \text{XO}^-] \cdot \alpha_{\text{H}^+}}{[\equiv \text{XOH}]} \quad (4)$$



**Table 3**  
Protonation Constants and Corresponding Site Concentrations  
Determined From Modelling of Acid-Base Titrations Data for the El Tatio  
Mud Samples

	logK	logK <sub>a-</sub>	logK <sub>a+</sub>	≡LH site density (mol/g)	≡XOH site density (mol/g)
Sample 1	3.79	-10.22	8.64	1.22 × 10 <sup>-04</sup>	6.55 × 10 <sup>-05</sup>
Sample 2	3.72	-11.74	8.83	1.14 × 10 <sup>-04</sup>	5.64 × 10 <sup>-05</sup>
Sample 3	3.72	-11.59	9.27	1.83 × 10 <sup>-04</sup>	1.36 × 10 <sup>-04</sup>
Sample 4	3.64	-9.60	8.06	1.16 × 10 <sup>-04</sup>	5.23 × 10 <sup>-05</sup>
Sample 5	3.73	-10.60	8.81	1.30 × 10 <sup>-04</sup>	7.12 × 10 <sup>-05</sup>

$$K_{a+} = \frac{[\equiv \text{XOH}_2^+]}{[\equiv \text{XOH}] \cdot \alpha_{\text{H}^+}} \quad (5)$$

The ≡LNa site represents surface functional groups generated by isomorphous substitution which have an inherent negative charge, while ≡XOH indicates amphoteric ≡Al-OH or ≡Si-OH groups that can either protonate or deprotonate.

The modeled surface functional group densities and protonation constants (logK, logK<sub>a+</sub>, and logK<sub>a-</sub>) are given in Table 3. Briefly, the site density of the ≡LH group is higher than that of the ≡XOH group, which ranges from 1.14 × 10<sup>-4</sup> to 1.83 × 10<sup>-4</sup> mol/g for the ≡LH group compared to 5.23 × 10<sup>-5</sup> to 1.36 × 10<sup>-4</sup> mol/g for the ≡XOH group. There is little discrepancy in the ion exchange reactions of ≡LH groups amongst the

five studied samples, with logK values ranging from 3.64 to 3.79. However, logK<sub>a-</sub> is greater for samples 1, 4, and 5 (-10.22, -9.60, and -10.60, respectively) than for samples 2 and 3 (-11.74 and -11.59, respectively). Sample 3 has the highest logK<sub>a+</sub> (9.27), followed by sample 2 (8.83), while samples 1, 2, and 4 have relatively lower logK<sub>a+</sub> (8.64, 8.06, and 8.81).

The variation of surface functional group speciation with solution pH is illustrated in Figure 7. Generally, ≡LH and ≡XOH<sub>2</sub><sup>+</sup> species dominate at low pH conditions (pH = 3–5), but the ≡LH group begins undergoing an ion exchange reaction with Na<sup>+</sup> at pH around 5 and ≡LNa species begin to dominate at pH higher than 7. The surface ≡XOH group is highly protonated as ≡XOH<sub>2</sub><sup>+</sup> over a wide pH range (pH = 3 to approximately 8). At pH higher than 8, aqueous species ≡XOH and ≡XO<sup>-</sup> begin to dominate; however, the pK<sub>a</sub> values of the second deprotonation reaction vary widely between 9.6 and 11.7. Thus, over the titrated pH range, the ≡XO<sup>-</sup> species is of minor importance in samples 2 and 3 but becomes important in samples 1, 4, and 5 at pH > 9. This indicates that the ≡XOH group in samples 2 and 3 has a higher proton affinity than in samples 1, 4, and 5.

The results of SCMs of acid-base titration data from ETGF mud samples (Table 3) are within the range of previously published proton binding constants and site concentrations for clay minerals (Baeyens & Bradbury, 1997; Barbier et al., 2000; Gu et al., 2010; Gu & Evans, 2007, 2008; Hao, Flynn, et al., 2019). Amongst our ETGF samples, sample 4 was collected from the lowest pH environment. It has the lowest logK (3.64) and logK<sub>a+</sub> (8.06) but highest logK<sub>a-</sub> (-9.60), which indicates that the acidic environment can lower the proton affinities of mineral surfaces. The overall surface functional group density of sample 4 is relatively low when compared to the other four samples. These data correspond to a previous study that showed that acidic treatment on clay minerals can decrease pK<sub>a</sub> values and surface functional group density (Jeon & Nam, 2019).

The surface functional group protonation diagrams for ETGF samples (Figure 7) indicate that ion-exchange reactions on ≡LH primarily occur between pH values of 5–6, where aqueous cations (such as Na<sup>+</sup> and Li<sup>+</sup>) can exchange with the interlayer of smectites. This can explain why a large portion of Li and Na can be released during acidic treatment (Table 2 and Figure 6). Acidic leaching can result in significant cationic elements release from the interlayers of clay minerals such as smectites, as evident in the leaching experiments with Na, Ca, Co, Sr, and Ba, where the protonation of amphoteric silanol and aluminol groups to ≡XOH<sub>2</sub><sup>+</sup> causes them to become repulsive to cations. While a highly protonated ≡XOH<sub>2</sub><sup>+</sup> surface speciation at lower pH attracts anions, when solution pH increases to values of 8–9, ≡XOH<sub>2</sub><sup>+</sup> progressively deprotonates to neutrally charged or negatively charged surface species. This then facilitates the desorption of anions, such as P and As, from clay mineral surfaces. As mentioned above, there may be minor mineral dissolution at low pH, which could also lead to trace elemental release.

Besides surface protonation/deprotonation reactions, hydrolysis reactions may also control the behavior of trace elements. Hydrolysis is, likewise, pH-dependent (e.g., Coup & Swedlund, 2015). For example, the hydrolysis of Cd at pH > 9 can change the Cd species from Cd<sup>2+</sup> to Cd(OH)<sub>2</sub><sup>0</sup>, and the latter can easily form

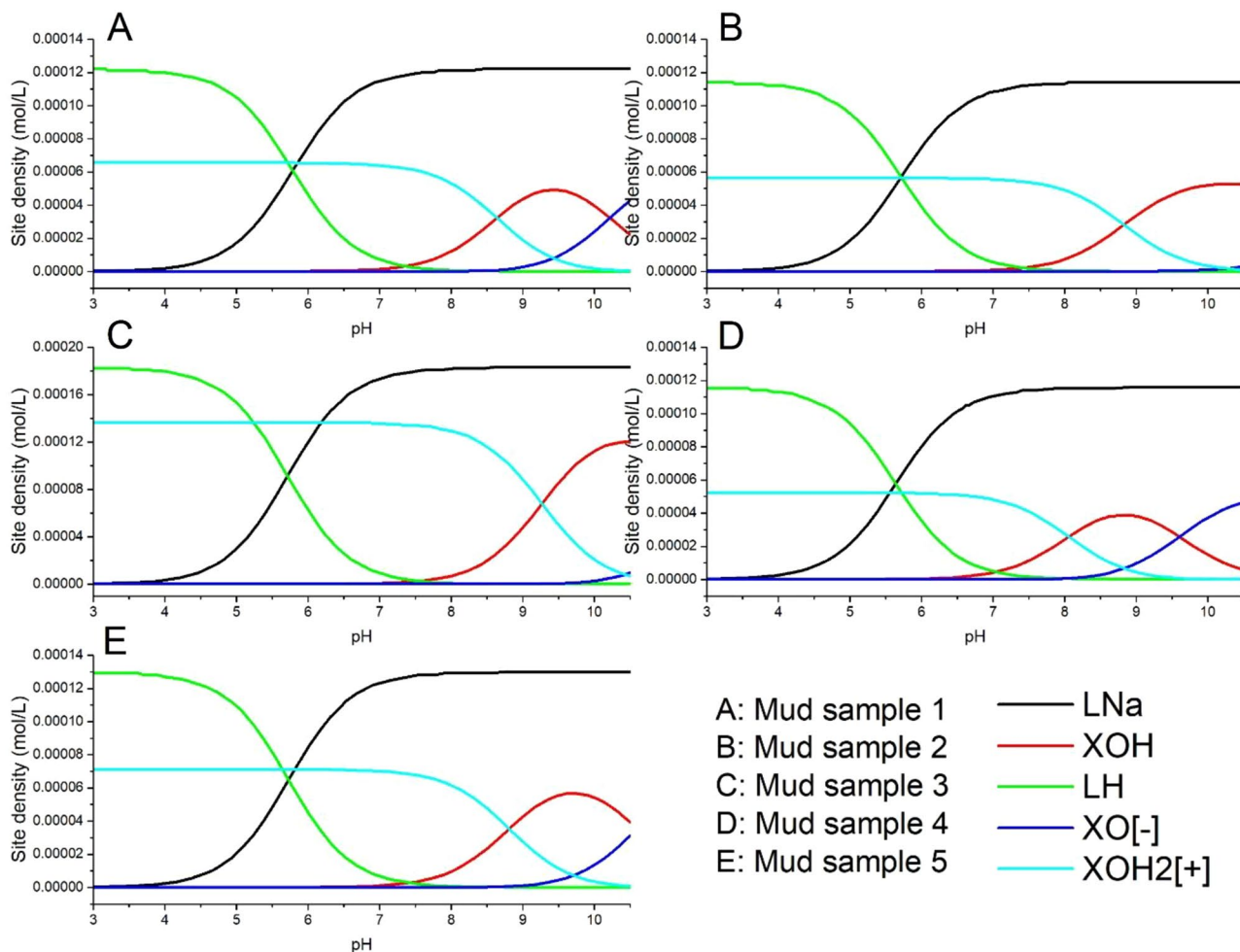


**Figure 7.** Surface functional group speciation diagrams for the five mud samples. The  $\equiv\text{LNa}$  group represents a surface group generated by isomorphous substitution and occupied by  $\text{Na}^+$  which has an inherently negative charge. The  $\equiv\text{LH}$  group is the protonated state of  $\equiv\text{LNa}$ ;  $\equiv\text{XOH}$  represents amphoteric  $\equiv\text{Al-OH}$  and  $\equiv\text{Si-OH}$  groups;  $\equiv\text{XO}^-$  and  $\equiv\text{XOH}_2^+$  are the deprotonated and protonated states of  $\equiv\text{XOH}$ , respectively.

inner-sphere complexes on clay surfaces and thus increase the adsorption of Cd on clays (Hao et al., 2020). Further, hydrolysis of Cd can lead to the formation of hydroxide secondary precipitates, such as  $\text{Cd}(\text{OH})_2$ , which is susceptible to dissolution under acidic conditions. Similar hydrolysis reactions also apply to Zn, Fe, Ca, and Mg, wherein increases in pH could lead to the hydrolysis of these cations and control their behavior on mud surfaces.

Based on the estimates of surface site density, the maximum concentrations of elements that can be adsorbed are  $1.87 \times 10^{-4}$ ,  $1.7 \times 10^{-4}$ ,  $1.97 \times 10^{-4}$ ,  $1.68 \times 10^{-4}$ , and  $2.01 \times 10^{-4}$  mol/g (the sum of concentrations for both sites) for the five mud samples, respectively. Normally adsorbed elements are weakly bound and subject to desorption if solution pH changes. However, during acid-base leaching experiments, we observed slightly more elemental release; for example, the sum of elemental release in acid and base treatment is  $12.90 \times 10^{-4}$ ,  $5.35 \times 10^{-4}$ ,  $7.32 \times 10^{-4}$ ,  $4.27 \times 10^{-4}$ , and  $3.79 \times 10^{-4}$  mol/g for the five mud samples, respectively (see Table S5). While some of the elements would be released under both acidic and alkaline conditions, we attribute the extra release of elements to the dissolution of minor minerals as discussed above. While we do not see such a change in the XRD spectra, this could be attributed to the presence of amorphous phases in the mud samples containing these elements, or crystalline phases that are not sufficiently abundant for detection by XRD.

## 6. Implications

The El Tatio geothermal field effluent drains westward to form the major headwaters for Region II, Chile (e.g., Rio Salado, which flows into the Rio Loa), containing high concentrations of Li, As, Mo, and Cd sourced from the geothermal water (Romero et al., 2003). Previous work focused on downstream attenuation of As via adsorption onto iron oxide surfaces (Landrum et al., 2009; Romero et al., 2003); however, our results show that these elements are also highly prone to be released from clay minerals into solution when subjected to upward environmental pH shifts on its journey from acidic sources, through circumneutral geothermal drainages, and eventually, alkaline seawater. Focusing specifically on As, previous sequential extraction analyses have shown that ~20% of As in Rio Loa Basin sediments is present in adsorbed fractions that readily exchange with water (Romero et al., 2003). We suggest that mud-bound As plays an important part of this readily exchanged fraction, and the release of weakly bound As from mud surfaces could contribute to the high concentration of As in the fluvial basin. For example, the suspension of 0.5 g/L of mud sample 1 (which has 4.2 mg of As per g of mud, 77.88% of which will be released as pH rises) in rivers will result in 1.65 mg/L of As in rivers, which is close to the As concentration in Rio Salado (1.1–1.2 mg/L; Romero et al., 2003). Due to the lack of dilution by freshwater in the Atacama Desert (Cappacconi et al., 2009), As contamination in Rio Salado can be traced several hundreds of km downstream; the lower part of Rio Loa has As concentrations ranging from 1.82 to 2.40 mg/L (Bugueño et al., 2014). It is worth noting that previous studies showed that the pH of river water in the ETGF area stays between 7 and 8 throughout the drainage basin (Romero et al., 2003), which indicates that the As desorption will occur in situ once the more acidic, As-bearing mud encounters relatively dilute, circumneutral river water, and the dissolved As will travel downstream.

Our research highlights how clay minerals can accumulate trace elements (e.g., As, P, Cd, Ca, Co, Sr, and Mo) in hydrothermal hot springs and subsequently release them into an aqueous solution with variations in environmental conditions. These findings confirm that the reactive and dynamic character of clay mineral surfaces affects aqueous chemistry in complex natural settings. Therefore, a nuanced assessment of the solid phase trace elements budget must be considered crucial in investigating environmental nutrient and pollutant fluxes.

## Data Availability Statement

Data sets are available online (<http://dx.doi.org/10.17632/x2788w327h.1>).

## Acknowledgments

This study was supported by NSERC Discovery Grants to K. O. Konhauser (RGPIN-165831), D. S. Alessi (RGPIN-04134), and S. A. Wilson (RGPIN-04368/RGPAS-00064). M. Van Zuilen acknowledges support from the European Research Council, under the European Union's Horizon 2020 Research and Innovation Program (Grant agreement no. 694894). The authors thank Rebecca Funk for collecting XRD patterns in the Department of Earth and Atmospheric Sciences X-ray Diffraction Laboratory.

## References

- Adriaens, A., Goossens, D., Pijpers, A., Van Tendeloo, G., & Gijbels, R. (1999). Dissolution study of potassium feldspars using hydrothermally treated sanidine as an example. *Surface and Interface Analysis*, 27, 8–23. [https://doi.org/10.1002/\(sici\)1096-9918\(199901\)27:1<8::aid-sia456>3.0.co;2-z](https://doi.org/10.1002/(sici)1096-9918(199901)27:1<8::aid-sia456>3.0.co;2-z)
- Allard, P., Aiuppa, A., Loyer, H., Carrot, F., Gaudry, A., Pinte, G., et al. (2000). Acid gas and metal emission rates during long-lived basalt degassing at Stromboli Volcano. *Geophysical Research Letters*, 27, 1207–1210. <https://doi.org/10.1029/1999gl008413>
- Alsina, M. A., Zanella, L., Hoel, C., Pizarro, G. E., Gaillard, J.-F., & Pasten, P. A. (2014). Arsenic speciation in sinter mineralization from a hydrothermal channel of El Tatio geothermal field, Chile. *Journal of Hydrology*, 518, 434–446. <https://doi.org/10.1016/j.jhydrol.2013.04.012>
- Angove, M. J., Johnson, B. B., & Wells, J. D. (1998). The influence of temperature on the adsorption of cadmium (II) and cobalt (II) on kaolinite. *Journal of Colloid and Interface Science*, 204(1), 93–103. <https://doi.org/10.1006/jcis.1998.5549>
- Bachmaf, S., & Merkel, B. J. (2011). Sorption of uranium (VI) at the clay mineral-water interface. *Environmental Earth Sciences*, 63(5), 925–934. <https://doi.org/10.1007/s12665-010-0761-6>
- Baeyens, B., & Bradbury, M. H. (1997). A mechanistic description of Ni and Zn sorption on Na-montmorillonite. 1. Titration and sorption measurements. *Journal of Contaminant Hydrology*, 27(3–4), 199–222. [https://doi.org/10.1016/s0169-7722\(97\)00008-9](https://doi.org/10.1016/s0169-7722(97)00008-9)
- Barbier, F., Duc, G., & Petit-Ramel, M. (2000). Adsorption of lead and cadmium ions from aqueous solution to the montmorillonite/water interface. *Colloids and Surfaces A: Physicochemical and Engineering Aspects*, 166(1–3), 153–159. [https://doi.org/10.1016/s0927-7757\(99\)00501-4](https://doi.org/10.1016/s0927-7757(99)00501-4)
- Bish, D. L., & Howard, S. A. (1988). Quantitative phase analysis using the Rietveld method. *Journal of Applied Crystallography*, 21, 86–91. <https://doi.org/10.1107/s0021889887009415>
- Bish, D. L., William Carey, J., Vaniman, D. T., & Chipera, S. J. (2003). Stability of hydrous minerals on the martian surface. *Icarus*, 164(1), 96–103. [https://doi.org/10.1016/s0019-1035\(03\)00140-4](https://doi.org/10.1016/s0019-1035(03)00140-4)
- Bradbury, M. H., & Baeyens, B. (2002). Sorption of Eu on Na- and Ca-montmorillonites: Experimental investigations and modelling with cation exchange and surface complexation. *Geochimica et Cosmochimica Acta*, 66(13), 2325–2334. [https://doi.org/10.1016/s0016-7037\(02\)00841-4](https://doi.org/10.1016/s0016-7037(02)00841-4)
- Bradbury, M. H., & Baeyens, B. (2009). Sorption modelling on illite Part I: Titration measurements and the sorption of Ni, Co, Eu and Sn. *Geochimica et Cosmochimica Acta*, 73(4), 990–1003. <https://doi.org/10.1016/j.gca.2008.11.017>

- Bugueño, M. P., Acevedo, S. E., Bonilla, C. A., Pizarro, G. E., & Pasten, P. A. (2014). Differential arsenic binding in the sediments of two sites in Chile's lower Loa River basin. *The Science of the Total Environment*, 466–467, 387–396. <https://doi.org/10.1016/j.scitotenv.2013.06.114>
- Capaccioni, B., Rossi, P. L., Tassi, F., & Aguilera, F. (2009). Origin and environmental impact of fluid discharges from the El Tatio geothermal field (Antofagasta region, Northern Chile). Geological constraints on the onset and evolution of an extreme environment: The Atacama area (Vol. 2, pp. 59–73). GeoActa Special Publication.
- Cardenas, M. B., & Engel, A. S. (2012). *Archaea at the El Tatio Geyser Field: Community composition, diversity, and distribution across hydrothermal features and geochemical gradients*.
- Catalano, J. G., & Brown, G. E. (2005). Uranyl adsorption onto montmorillonite: Evaluation of binding sites and carbonate complexation. *Geochimica et Cosmochimica Acta*, 69(12), 2995–3005. <https://doi.org/10.1016/j.gca.2005.01.025>
- Cheary, R. W., & Coelho, A. (1992). A fundamental parameters approach to x-ray line-profile fitting. *Journal of Applied Crystallography*, 25, 109–121. <https://doi.org/10.1107/s0021889891010804>
- Cortecchi, G., Boschetti, T., Mussi, M., Lameli, C. H., Mucchino, C., & Barbieri, M. (2005). New chemical and original isotopic data on waters from El Tatio geothermal field, northern Chile. *Geochemical Journal*, 39(6), 547–571. <https://doi.org/10.2343/geochemj.39.547>
- Coup, K. M., & Swedlund, P. J. (2015). Demystifying the interfacial aquatic geochemistry of thallium(I): New and old data reveal just a regular cation. *Chemical Geology*, 398, 97–103. <https://doi.org/10.1016/j.chemgeo.2015.02.003>
- Cusicanqui, H., Mahon, W. A. J., & Ellis, A. J. (1976). *The geochemistry of the El Tatio geothermal field, Northern Chile*.
- De Silva, S. L. (1989). Altiplano-Puna volcanic complex of the central Andes. *Geology*, 17(12), 1102–1106. [https://doi.org/10.1130/0091-7613\(1989\)017<1102:apvcot>2.3.co;2](https://doi.org/10.1130/0091-7613(1989)017<1102:apvcot>2.3.co;2)
- De Silva, S. L., & Francis, P. (1991). *Volcanoes of the central Andes* (p. 219). Springer-Verlag Berlin.
- De Silva, S. L., Self, S., Francis, P. W., Drake, R. E., & Carlos, R. R. (1994). Effusive silicic volcanism in the Central Andes: The Chao dacite and other young lavas of the Altiplano-Puna volcanic complex. *Journal of Geophysical Research*, 99(B9), 17805–17825. <https://doi.org/10.1029/94jb00652>
- Edmonds, M., Mather, T. A., & Liu, E. J. (2018). A distinct metal fingerprint in arc volcanic emissions. *Nature Geoscience*, 11, 790–794. <https://doi.org/10.1038/s41561-018-0214-5>
- Ellis, A. (1969). Survey for geothermal development in Northern Chile. *Preliminary geochemistry report, El Tatio geothermal field*. UNDP-Report.
- Ellis, A. J., & Mahon, W. A. J. (1964). Natural hydrothermal systems and experimental hot-water/rock interactions. *Geochimica et Cosmochimica Acta*, 28(8), 1323–1357. [https://doi.org/10.1016/0016-7037\(64\)90132-2](https://doi.org/10.1016/0016-7037(64)90132-2)
- Ellis, A. J., & Mahon, W. A. J. (1967). Natural hydrothermal systems and experimental hot water/rock interactions (Part II). *Geochimica et Cosmochimica Acta*, 31(4), 519–538. [https://doi.org/10.1016/0016-7037\(67\)90032-4](https://doi.org/10.1016/0016-7037(67)90032-4)
- Engel, A. S., Johnson, L. R., & Porter, M. L. (2013). Arsenite oxidase gene diversity among Chloroflexi and Proteobacteria from El Tatio Geyser Field, Chile. *FEMS Microbiology Ecology*, 83(3), 745–756. <https://doi.org/10.1111/1574-6941.12030>
- Escudero, L. V., Casamayor, E. O., Chong, G., Pedrós-Alió, C., & Demergasso, C. (2013). Distribution of microbial arsenic reduction, oxidation and extrusion genes along a wide range of environmental arsenic concentrations. *PLoS One*, 8(10), e78890. <https://doi.org/10.1371/journal.pone.0078890>
- Fernandez-Turiel, J. L., Garcia-Valles, M., Gimeno-Torrente, D., Saavedra-Alonso, J., & Martinez-Manent, S. (2005). The hot spring and geyser sinters of El Tatio, Northern Chile. *Sedimentary Geology*, 180(3), 125–147. <https://doi.org/10.1016/j.sedgeo.2005.07.005>
- Fuller, A. J., Shaw, S., Ward, M. B., Haigh, S. J., Mosselmans, J. F. W., Peacock, C. L., et al. (2015). Caesium incorporation and retention in illite interlayers. *Applied Clay Science*, 108, 128–134. <https://doi.org/10.1016/j.clay.2015.02.008>
- García-Valles, M., Fernández-Turiel, J., Gimeno-Torrente, D., Saavedra-Alonso, J., & Martínez-Manent, S. (2008). Mineralogical characterization of silica sinters from the El Tatio geothermal field, Chile. *American Mineralogist*, 93(8–9), 1373–1383. <https://doi.org/10.2138/am.2008.2583>
- Gérard, F. (2016). Clay minerals, iron/aluminum oxides, and their contribution to phosphate sorption in soils – A myth revisited. *Geoderma*, 262, 213–226. <https://doi.org/10.1016/j.geoderma.2015.08.036>
- Giggenbach, W. F. (1978). The isotopic composition of waters from the El Tatio geothermal field, Northern Chile. *Geochimica et Cosmochimica Acta*, 42(7), 979–988. [https://doi.org/10.1016/0016-7037\(78\)90287-9](https://doi.org/10.1016/0016-7037(78)90287-9)
- Glennon, J. A., & Pfaff, R. M. (2003). The extraordinary thermal activity of El Tatio geyser field, Antofagasta Region, Chile. *GOSA Trans*, 8, 31–78.
- Goldberg, S. (2002). Competitive adsorption of arsenate and arsenite on oxides and clay minerals. *Soil Science Society of America Journal*, 66(2), 413–421. <https://doi.org/10.2136/sssaj2002.0413>
- Goldberg, S., Forster, H. S., & Godfrey, C. L. (1996). Molybdenum adsorption on oxides, clay minerals, and soils. *Soil Science Society of America Journal*, 60(2), 425–432. <https://doi.org/10.2136/sssaj1996.03615995006000020013x>
- Gong, J., Myers, K. D., Munoz-Saez, C., Homann, M., Rouillard, J., Wirth, R., et al. (2019). Formation and preservation of microbial palisade fabric in silica deposits from El Tatio, Chile. *Astrobiology*, 20(4), 500–524. <https://doi.org/10.1089/ast.2019.2025>
- Gualtieri, A. F. (2000). Accuracy of XRPD QPA using the combined Rietveld-RIR method. *Journal of Applied Crystallography*, 33, 267–278. <https://doi.org/10.1107/s002188989901643x>
- Gu, X., & Evans, L. J. (2007). Modelling the adsorption of Cd(II), Cu(II), Ni(II), Pb(II), and Zn(II) onto Fithian illite. *Journal of Colloid and Interface Science*, 307(2), 317–325. <https://doi.org/10.1016/j.jcis.2006.11.022>
- Gu, X., & Evans, L. J. (2008). Surface complexation modelling of Cd(II), Cu(II), Ni(II), Pb(II) and Zn(II) adsorption onto kaolinite. *Geochimica et Cosmochimica Acta*, 72(2), 267–276. <https://doi.org/10.1016/j.gca.2007.09.032>
- Gu, X., Evans, L. J., & Barabash, S. J. (2010). Modeling the adsorption of Cd (II), Cu (II), Ni (II), Pb (II) and Zn (II) onto montmorillonite. *Geochimica et Cosmochimica Acta*, 74(20), 5718–5728. <https://doi.org/10.1016/j.gca.2010.07.016>
- Hao, W., Flynn, S. L., Alessi, D. S., & Konhauser, K. O. (2018). Change of the point of zero net proton charge (pHPZNPC) of clay minerals with ionic strength. *Chemical Geology*, 493, 458–467. <https://doi.org/10.1016/j.chemgeo.2018.06.023>
- Hao, W., Flynn, S. L., Kashiwabara, T., Alam, M. S., Bandara, S., Swaren, L., et al. (2019). The impact of ionic strength on the proton reactivity of clay minerals. *Chemical Geology*, 529, 119294. <https://doi.org/10.1016/j.chemgeo.2019.119294>
- Hao, W., Kashiwabara, T., Jin, R., Takahashi, Y., Gingras, M., Alessi, D. S., & Konhauser, K. O. (2020). Clay minerals as a source of cadmium to estuaries. *Scientific Reports*, 10, 10417. <https://doi.org/10.1038/s41598-020-67279-w>
- Hao, W., Pudasainee, D., Gupta, R., Kashiwabara, T., Alessi, D. S., & Konhauser, K. O. (2019). Effect of acidic conditions on surface properties and metal binding capacity of clay minerals. *ACS Earth and Space Chemistry*, 3, 2421–2429. <https://doi.org/10.1021/acsearthspacechem.9b00166>

- Healy, J., & Hochstein, M. (1973). Horizontal flow in hydrothermal systems. *Journal of Hydrology*, 12(2), 71–82. <https://www.jstor.org/stable/43944276>
- Hill, R. J., & Howard, C. J. (1987). Quantitative phase analysis from neutron powder diffraction data using the Rietveld method. *Journal of Applied Crystallography*, 20, 467–474. <https://doi.org/10.1107/s0021889887086199>
- Ikhshan, J., Wells, J. D., Johnson, B. B., & Angove, M. J. (2005). Surface complexation modeling of the sorption of Zn(II) by montmorillonite. *Colloids and Surfaces A: Physicochemical and Engineering Aspects*, 252(1), 33–41. <https://doi.org/10.1016/j.colsurfa.2004.10.011>
- Jeong, C. H. (2001). Mineralogical and hydrochemical effects on adsorption removal of cesium-137 and strontium-90 by kaolinite. *Journal of Environmental Science and Health, Part A*, 36(6), 1089–1099. <https://doi.org/10.1081/ese-100104133>
- Jeon, I., & Nam, K. (2019). Change in the site density and surface acidity of clay minerals by acid or alkali spills and its effect on pH buffering capacity. *Scientific Reports*, 9(1), 9878. <https://doi.org/10.1038/s41598-019-46175-y>
- Kosmulski, M. (2011). The pH-dependent surface charging and points of zero charge. *Journal of Colloid and Interface Science*, 353, 1–15. <https://doi.org/10.1016/j.jcis.2010.08.023>
- Krepelova, A., Reich, T., Sachs, S., Drebert, J., & Bernhard, G. (2008). Structural characterization of U(VI) surface complexes on kaolinite in the presence of humic acid using EXAFS spectroscopy. *Journal of Colloid and Interface Science*, 319(1), 40–47. <https://doi.org/10.1016/j.jcis.2007.11.010>
- Lackovic, K., Angove, M. J., Wells, J. D., & Johnson, B. B. (2003). Modeling the adsorption of Cd(II) onto Muloorina illite and related clay minerals. *Journal of Colloid and Interface Science*, 257(1), 31–40. [https://doi.org/10.1016/s0021-9797\(02\)00031-0](https://doi.org/10.1016/s0021-9797(02)00031-0)
- Lahsen, A. (1988). Chilean geothermal resources and their possible utilization. *Geothermics*, 17(2–3), 401–410. [https://doi.org/10.1016/0375-6505\(88\)90068-5](https://doi.org/10.1016/0375-6505(88)90068-5)
- Lahsen, A., & Trujillo, P. (1976). The geothermal field of El Tatio, Chile. *Paper presented at second United Nations symposium on the development and use of geothermal resources*. (pp. 170–177).
- Landrum, J. T., Bennett, P. C., Engel, A. S., Alsina, M. A., Pastén, P. A., & Milliken, K. (2009). Partitioning geochemistry of arsenic and antimony, El Tatio Geysers Field, Chile. *Applied Geochemistry*, 24(4), 664–676. <https://doi.org/10.1016/j.apgeochem.2008.12.024>
- Landry, C. J., Koretsky, C. M., Lund, T. J., Schaller, M., & Das, S. (2009). Surface complexation modeling of Co(II) adsorption on mixtures of hydrous ferric oxide, quartz and kaolinite. *Geochimica et Cosmochimica Acta*, 73(13), 3723–3737. <https://doi.org/10.1016/j.gca.2009.03.028>
- Leiva, E. D., Rámila, C. d. P., Vargas, I. T., Escarriaza, C. R., Bonilla, C. A., Pizarro, G. E., et al. (2014). Natural attenuation process via microbial oxidation of arsenic in a high Andean watershed. *The Science of the Total Environment*, 466–467, 490–502. <https://doi.org/10.1016/j.scitotenv.2013.07.009>
- Liu, C.-C., Jean, J.-S., Nath, B., Lee, M.-K., Hor, L.-I., Lin, K.-H., & Maity, J. P. (2009). Geochemical characteristics of the fluids and muds from two southern Taiwan mud volcanoes: Implications for water-sediment interaction and groundwater arsenic enrichment. *Applied Geochemistry*, 24(9), 1793–1802. <https://doi.org/10.1016/j.apgeochem.2009.06.002>
- Liu, Y., Alessi, D. S., Flynn, S. L., Alam, M. S., Hao, W., Gingras, M., et al. (2018). Acid-base properties of kaolinite, montmorillonite and illite at marine ionic strength. *Chemical Geology*, 483, 191–200. <https://doi.org/10.1016/j.chemgeo.2018.01.018>
- Locock, A. J., Chesterman, D., Caird, D., & Duke, M. J. M. (2012). Miniaturization of mechanical milling for powder X-ray diffraction. *Powder Diffraction*, 27(3), 189–193. <https://doi.org/10.1017/s0885715612000516>
- Lützenkirchen, J., Preočanin, T., Kovačević, D., Tomišić, V., Lövgren, L., & Kallay, N. (2012). Potentiometric titrations as a tool for surface charge determination. *Croatica Chemica Acta*, 85(4), 391–417. <https://doi.org/10.5562/cca2062>
- Magaritz, M., Aravena, R., Peña, H., Suzuki, O., & Grilli, A. (1990). Source of ground water in the deserts of northern Chile: Evidence of deep circulation of ground water from the Andes. *Ground Water*, 28(4), 513–517. <https://doi.org/10.1111/j.1745-6584.1990.tb01706.x>
- Mather, T. A., Witt, M. L. I., Pyle, D. M., Quayle, B. M., Aiuppa, A., Bagnato, E., et al. (2012). Halogens and trace metal emissions from the ongoing 2008 summit eruption of Kilauea volcano, Hawai'i. *Geochimica et Cosmochimica Acta*, 83, 292–323. <https://doi.org/10.1016/j.gca.2011.11.029>
- Mervine, E. M., Wilson, S. A., Power, I. M., Dipple, G. M., Turvey, C. C., Hamilton, J. L., et al. (2018). Potential for offsetting diamond mine carbon emissions through mineral carbonation of processed kimberlite: An assessment of De Beers mine sites in South Africa and Canada. *Mineralogy and Petrology*, 112, 755–765. <https://doi.org/10.1007/s00710-018-0589-4>
- Morteani, G., Möller, P., Dulski, P., & Preinfalk, C. (2014). Major, trace element and stable isotope composition of water and muds precipitated from the hot springs of Bolivia: Are the waters of the spring's potential ore forming fluids? *Geochemistry*, 74(1), 49–62. <https://doi.org/10.1016/j.chemer.2013.06.002>
- Mountain, B. W., Benning, L. G., & Graham, D. J. (2001). Biomineralization in New Zealand geothermal areas. *Paper presented at 23rd New Zealand geothermal workshop*. (pp. 27–32).
- Munoz-Saez, C., Manga, M., & Hurwitz, S. (2018). Hydrothermal discharge from the El Tatio basin, Atacama, Chile. *Journal of Volcanology and Geothermal Research*, 361, 25–35. <https://doi.org/10.1016/j.jvolgeores.2018.07.007>
- Munoz-Saez, C., Namiki, A., & Manga, M. (2015). Geysers eruption intervals and interactions: Examples from El Tatio, Atacama, Chile. *Journal of Geophysical Research: Solid Earth*, 120, 7490–7507. <https://doi.org/10.1002/2015jb012364>
- Munoz-Saez, C., Saltiel, S., Manga, M., Nguyen, C., & Gonnermann, H. (2016). Physical and hydraulic properties of modern sinter deposits: El Tatio, Atacama. *Journal of Volcanology and Geothermal Research*, 325, 156–168. <https://doi.org/10.1016/j.jvolgeores.2016.06.026>
- Myers, K. D. (2015). *The microbial ecology and biogeochemistry of cyanobacteria in the arsenic-rich and inorganic carbon-limited geothermal waters of El Tatio Geysers Field, Chile*. The University of Texas at Austin.
- Nicolau, C., Reich, M., & Lynne, B. (2014). Physico-chemical and environmental controls on siliceous sinter formation at the high-altitude El Tatio geothermal field, Chile. *Journal of Volcanology and Geothermal Research*, 282, 60–76. <https://doi.org/10.1016/j.jvolgeores.2014.06.012>
- Peacock, C. L., & Sherman, D. M. (2005). Surface complexation model for multisite adsorption of copper(II) onto kaolinite. *Geochimica et Cosmochimica Acta*, 69(15), 3733–3745. <https://doi.org/10.1016/j.gca.2004.12.029>
- Phoenix, V. R., Bennett, P. C., Engel, A. S., Tyler, S. W., & Ferris, F. G. (2006). Chilean high-altitude hot-spring sinters: A model system for UV screening mechanisms by early Precambrian cyanobacteria. *Geobiology*, 4(1), 15–28. <https://doi.org/10.1111/j.1472-4669.2006.00063.x>
- Plenge, M. F., Engel, A. S., Omelon, C. R., & Bennett, P. C. (2017). Thermophilic archaeal diversity and methanogenesis from El Tatio Geysers Field, Chile. *Geomicrobiology Journal*, 34(3), 220–230. <https://doi.org/10.1080/01490451.2016.1168496>
- Rietveld, H. M. (1969). A profile refinement method for nuclear and magnetic structures. *Journal of Applied Crystallography*, 2, 65–71. <https://doi.org/10.1107/s0021889869006558>

- Rodgers, K. A., Greatrex, R., Hyland, M., Simmons, S. F., & Browne, P. R. L. (2002). A modern, evaporitic occurrence of teruggite,  $\text{Ca}_2\text{Mg-B}_{12}\text{As}_2\text{O}_{28}\cdot 18\text{H}_2\text{O}$ , and nobleite,  $\text{CaB}_6\text{O}_{10}\cdot 4\text{H}_2\text{O}$ , from the El Tatio geothermal field, Antofagasta Province, Chile. *Mineralogical Magazine*, 66(2), 253–259. <https://doi.org/10.1180/0026461026620026>
- Romero, L., Alonso, H., Campano, P., Fanfani, L., Cidu, R., Dadea, C., et al. (2003). Arsenic enrichment in waters and sediments of the Rio Loa (Second Region, Chile). *Applied Geochemistry*, 18(9), 1399–1416. [https://doi.org/10.1016/s0883-2927\(03\)00059-3](https://doi.org/10.1016/s0883-2927(03)00059-3)
- Sahai, N., & Sverjensky, D. A. (1997). Solvation and electrostatic model for specific electrolyte adsorption. *Geochimica et Cosmochimica Acta*, 61(14), 2827–2848. [https://doi.org/10.1016/s0016-7037\(97\)00127-0](https://doi.org/10.1016/s0016-7037(97)00127-0)
- Sanchez-Garcia, L., Fernandez-Martinez, M. A., Garcia-Villadangos, M., Blanco, Y., Cady, S. L., Hinman, N., et al. (2019). Microbial biomarker transition in high-altitude sinter mounds from El Tatio (Chile) through different stages of hydrothermal activity. *Frontiers in Microbiology*, 9(3350). <https://doi.org/10.3389/fmicb.2018.03350>
- Scarlett, N. V. Y., & Madsen, I. C. (2006). Quantification of phases with partial or no known crystal structures. *Powder Diffraction*, 21(4), 278–284. <https://doi.org/10.1154/1.2362855>
- Schlegel, M. L., & Descostes, M. (2009). Uranium uptake by hectorite and montmorillonite: A solution chemistry and polarized EXAFS study. *Environmental Science & Technology*, 43(22), 8593–8598. <https://doi.org/10.1021/es902001k>
- Scott, A. D., & Smith, S. J. (1966). Susceptibility of interlayer potassium in micas to exchange with sodium, Clays and clay minerals (pp. 69–81). Elsevier. <https://doi.org/10.1016/b978-0-08-011908-3.50008-6>
- Smith, A. H., Marshall, G., Liaw, J., Yuan, Y., Ferreccio, C., & Steinmaus, C. (2012). Mortality in young adults following in utero and childhood exposure to arsenic in drinking water. *Environmental Health Perspectives*, 120(11), 1527–1531. <https://doi.org/10.1289/ehp.1104867>
- Sposito, G., Skipper, N. T., Sutton, R., Park, S.-H., Soper, A. K., & Greathouse, J. A. (1999). Surface geochemistry of the clay minerals. *Proceedings of the National Academy of Sciences of the United States of America*, 96(7), 3358–3364. <https://doi.org/10.1073/pnas.96.7.3358>
- Sverjensky, D. A., & Sahai, N. (1996). Theoretical prediction of single-site surface-protonation equilibrium constants for oxides and silicates in water. *Geochimica et Cosmochimica Acta*, 60(20), 3773–3797. [https://doi.org/10.1016/0016-7037\(96\)00207-4](https://doi.org/10.1016/0016-7037(96)00207-4)
- Tassi, F., Aguilera, F., Darrah, T., Vaselli, O., Capaccioni, B., Poreda, R. J., & Delgado Huertas, A. (2010). Fluid geochemistry of hydrothermal systems in the Arica-Parinacota, Tarapacá and Antofagasta regions (northern Chile). *Journal of Volcanology and Geothermal Research*, 192(1–2), 1–15. <https://doi.org/10.1016/j.jvolgeores.2010.02.006>
- Tassi, F., Aguilera, F., Vaselli, O., Medina, E., Tedesco, D., Delgado Huertas, A., et al. (2009). The magmatic- and hydrothermal-dominated fumarolic system at the Active Crater of Lascar volcano, northern Chile. *Bulletin of Volcanology*, 71(2), 171–183. <https://doi.org/10.1007/s00445-008-0216-z>
- Tournassat, C., Davis, J. A., Chiaberge, C., Grangeon, S., & Bourg, I. C. (2016). Modeling the acid-base properties of montmorillonite edge surfaces. *Environmental Science & Technology*, 50(24), 13436–13445. <https://doi.org/10.1021/acs.est.6b04677>
- Tournassat, C., Greneche, J.-M., Tisserand, D., & Charlet, L. (2004). The titration of clay minerals. *Journal of Colloid and Interface Science*, 273(1), 224–233. <https://doi.org/10.1016/j.jcis.2003.11.021>
- Turvey, C. C., Hamilton, J. L., & Wilson, S. A. (2018). Comparison of Rietveld-compatible structureless fitting analysis methods for accurate quantification of carbon dioxide fixation in ultramafic mine tailings. *American Mineralogist*, 103(10), 1649–1662. <https://doi.org/10.2138/am-2018-6515>
- Wilmeth, D. T., Nabhan, S., Myers, K. D., Slagter, S., Lalonde, S. V., Sansjofre, P., et al. (2020). Depositional evolution of an extinct sinter mound from source to outflow, El Tatio, Chile. *Sedimentary Geology*, 406, 105726. <https://doi.org/10.1016/j.sedgeo.2020.105726>
- Wilson, S. A., Raudsepp, M., & Dipple, G. M. (2006). Verifying and quantifying carbon fixation in minerals from serpentine-rich mine tailings using the Rietveld method with X-ray powder diffraction data. *American Mineralogist*, 91(8–9), 1331–1341. <https://doi.org/10.2138/am.2006.2058>
- Xue, N.-N., Zhang, Y.-M., Liu, T., & Huang, J. (2015). Study of the dissolution behavior of muscovite in stone coal by oxygen pressure acid leaching. *Metallurgical and Materials Transactions B*, 47, 694–701. <https://doi.org/10.1007/s11663-015-0524-6>